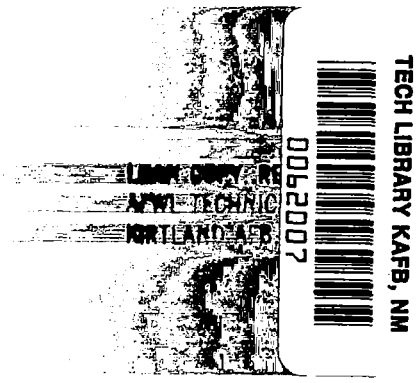

NASA Contractor Report 3455

Development of an Unsteady Aerodynamic Analysis for Finite-Deflection Subsonic Cascades

Joseph M. Verdon and Joseph R. Caspar

CONTRACT NAS3-21981
SEPTEMBER 1981

NASA

NASA Contractor Report 3455

Development of an Unsteady Aerodynamic Analysis for Finite-Deflection Subsonic Cascades

Joseph M. Verdon and Joseph R. Caspar
United Technologies Research Center
East Hartford, Connecticut

Prepared for
Lewis Research Center
under Contract NAS3-21981

NASA
National Aeronautics
and Space Administration

Scientific and Technical
Information Branch

1981

TABLE OF CONTENTS

TABLE OF CONTENTS (Concluded)

LIST OF SYMBOLS

Note: All quantities are dimensionless. Lengths have been scaled with respect to blade chord, time with respect to the ratio of blade chord to upstream free-stream speed, and pressure with respect to the upstream free-stream dynamic pressure.

Latin

$\mathcal{A}, \mathcal{B}$	matrix defining the least-spares fit, Eq. (34)
$A_\ell, B_\ell, C_\ell, d_\ell$	sub-matrix of block-tridiagonal system of difference equations, Eq. (45)
$\hat{A}$	speed of sound, Eq. (2)
A	zeroth-order or steady speed of sound
a	one-fourth of the distance between the foci of an ellipse, Eq. (A1)
b	thickness of elliptic airfoil, Eq. (A1)
$b_{j,\mp}$	far-field Fourier coefficient, Eq. (15)
$\mathcal{C}$	interpolating matrix, Eqs. (25) and (35)
$\hat{\vec{C}}_F$, $\hat{C}_M$	aerodynamic force, moment coefficient, Eqs. (20) and (21)
$\vec{C}_F$, C_M	zeroth-order or steady force, moment coefficient, Eq. (22)
$\vec{c}_F$, c_M	first-order or unsteady force, moment coefficient, Eq. (23)
$\underset{\sim}{c}^0$, $\underset{\sim}{c}^I$	interpolating vector which depends on neighbor set geometry, Eq. (25)
$\mathcal{D}$	extended blade-passage region (solution domain), Fig. 2
D_S/Dt	material or convective derivative relative to the zeroth-order or steady flow, Eq. (10)
$\vec{ds}$	differential vector tangent to mean blade surface, Eq. (22)

LIST OF SYMBOLS (Continued)

$e(\underset{\sim}{\gamma})$	error function, Eq. (31)
$e_c(\underset{\sim}{\gamma})$	constrained error function, Eq. (38)
$\vec{e}_x$, $\vec{e}_y$	unit vector in x, y-direction
$\mathcal{Q}$	MxN matrix with components consisting of the N interpolating functions evaluated at the M neighbor points, Eq. (34)
F	difference between unsteady potential at a given point and at calculation point, Eq. (24)
$F(\upsilon)$	function describing the discontinous unsteady behavior far downstream of the cascade, Eq. (16)
$F(\mathcal{Q}),G(\mathcal{Q}),H(\mathcal{Q},\hat{A})$	complex functions, Eqs. (A1) and (A2)
f^n	interpolating function, Eq. (24)
$\underset{\sim}{f}$	column vector with components f^n ,n=1,..., N, Eq. (24)
$\vec{G}$	cascade gap vector, Fig. 1
$g(\underset{\sim}{\gamma})$	complex constraint functional, Eq. (37)
$\mathcal{H}$	linear differential operator, Eq. (36)
H	scalar defined by Eq. (41)
h^0	zeroth-order coefficient of the differential operator $\mathcal{H}$, Eq. (37)
h^I	inhomogeneous part of the differential operator $\mathcal{H}$, Eq. (37)
$\vec{h}$	translational displacement vector, Eq. (4)
$\mathrm{Im}\{\ \}$	imaginary part of $\{\ \}$
i	imaginary unit

LIST OF SYMBOLS (Continued)

$\mathcal{L}$	linear differential operator, Eq. (26)
L	linear difference operator, Eq. (27)
M	zeroth-order or steady Mach number; number of neighbor points in calculation mesh
m	blade number (m=o denotes the reference blade)
N	number of interpolating functions used in least-squares difference approximation, Eq. (30)
$\vec{n}$	unit outward normal vector
$\mathcal{O}$	order symbol
$\hat{P}$	pressure, Eq. (2)
P	zeroth-order or steady pressure, Eq. (17)
$pe^{i\omega t}$	first-order or unsteady pressure, Eq. (17)
Q_m	mesh-point; m=0 refers to calculation point; m=1,...,M refers to neighboring mesh points
q^0	zeroth-order coefficient of the differential operator $\mathcal{L}$, Eq (26)
q_j	far-field constant, Eq. (14)
$\vec{\mathcal{R}}$	Blade displacement vector, Eq. (4)
$\vec{R}_p$	position vector extending from reference blade pitching (torsional) axis
Re{ }	real part of{ }
$\vec{r}$	displacement amplitude vector, Eq. (4)
r_e	distance from airfoil leading or trailing edge

LIST OF SYMBOLS (Continued)

$\mathcal{S}$	instantaneous position of reference blade surface
S	mean position of reference blade surface
s	scalar defined by Eq. (42); complex displacement, Eq. (A7)
T	blade thickness, Eq. (46)
t	time
$\vec{V}$	zeroth-order or steady velocity
$\mathcal{W}$	instantaneous position of reference wake surface
W	mean position of wake surface, Fig. 1; diagonal weighting function matrix, Eq. (34)
$\hat{W}(\zeta)$	complex potential of flow past displaced ellipse, Eq. (A1)
$W(z)$	zeroth order complex potential, Eq. (A3)
$w(z)$	first order complex potential, Eq. (A3)
w_m	weighting function, Eq. (32)
$\vec{X}$	position vector
Xp,Yp	coordinates of reference blade pitching (torsional) axis
ξ, η	cartesian coordinates with ξ-axis directed along major axis of displaced ellipse
x,y	cartesion coordinates with x-axis directed along mean position of blade chord, Fig. 1, or major axis of ellipse
ζ, z	body-fixed complex coordinate, Fig. 20
z_C	complex coordinate measured from center of leading edge circle (=z+2a)

LIST OF SYMBOLS (Continued)

z_{LE}	complex coordinate measured from leading edge (=Z+1/2)
Greek	
$\hat{A}$	angle of attack of displaced elliptic airfoil, Eq. (A1)
A	mean angle of attack, Eq. (A6)
$\vec{\alpha}$	rotational displacement vector, Eq. (4)
$\underset{\sim}{\beta}$	column vector defined by Eq. (28)
β_0, β_I	scalar defined by Eq. (28)
$\hat{\Gamma}$	circulation, Eq. (A2)
γ^n	interpolating coefficient, Eq. (24)
$\underset{\sim}{\gamma}$	column vector with components γ^n, n=1,...,N, Eqs. (24) and (25)
γ	specific heat ratio
Δp	unsteady pressure difference coefficient, Eq. (48)
$\Delta_m \phi e^{i\omega t}$	difference in unsteady potential across the mth wake, Eq. (13)
$\delta\xi$	axial distance between mesh points
$\delta\eta$	tangential (i.e. parallel to cascade inlet plane) distance between mesh points
$\delta\phi_m$	difference between values of ϕ at mth neighbor point and at calculation point
$\underset{\sim}{\delta\phi}$	column vector with components $\delta\phi_m$, m=1,...,M, Eq. (25)
ϵ, ϵ_S	small parameters, Eqs. (5) and (8)

η_+	η-coordinate of the point of intersection of the reference stagnation streamline and the line $\xi = \xi_+$, Fig. 2 and Eq. (16)
Θ	cascade stagger angle, Fig. 1
λ	Lagrange multiplier, Eq. (38)
ξ, η	cartesian coordinates with ξ-axis directed axially, Fig. 1
$\xi_{\mp}$	far upstream and downstream boundary locations, Fig. 2
σ	interblade phase angle, positive when motion of the (m+1)th blade leads the motion of the mth blade, Eq. (4)
τ, υ	cartesian coordinates, τ-axis coincides with assumed mean position of reference wake in the far-field, Fig. 2
$\hat{\Phi}$	velocity potential, Eq. (1)
Φ	zeroth-order or steady velocity potential, Eq. (5)
$\phi e^{i\omega t}$	first-order or unsteady velocity potential, Eq. (5)
$\phi_c e^{i\omega t}$	continuous component of far-field unsteady potential, Eq. (14)
$\phi_d e^{i\omega t}$	discontinuous component of far-downstream unsteady potential, Eq. (16)
$\chi_{j,\mp}$	far-field constant, Eq. (14)
$\Omega_{\mp\infty}$	far-upstream, downstream flow angle, Fig. 1
ω	frequency (circular) of blade motion, Eq. (4)

Superscripts

j	jth term of asymptotic series, Eq. (5)
n	column vector component

T	transpose
+,-	upper, lower surface of blade or wake
‾	complex conjugate
*	conjugate transposition

Subscripts

C	center of airfoil leading edge circle
E	leading or trailing edge of airfoil
LE	leading edge of airfoil
I	inner solution, Eq. (A20)
L	number of axial or radial mesh lines, Eq. (45)
ℓ	axial or radial mesh line, Eq. (45)
M	number of neighbor mesh points
m	blade number; neighboring mesh point
O	outer solution, Eq. (A23)
$\mathcal{S}$	instantaneous position of blade surface
S	mean position of blade surface
t	local time derivative, Eq. (1)
y	y-component of vector
0	calculation point
-,+	far upstream, downstream of blade row

LIST OF SYMBOLS (Concluded)

$-\infty,\infty$	upstream, downstream free-stream state
$\sim$	column vector

SUMMARY

An unsteady potential flow analysis, which accounts for the effects of blade geometry and steady turning, is being developed to predict aerodynamic forces and moments associated with free-vibration or flutter phenomena in the fan, compressor, or turbine stages of modern jet engines. Based on the assumption of small-amplitude blade motions, the unsteady flow is governed by linear equations with variable coefficients which depend on the underlying steady flow. These equations are approximated using difference expressions determined from an implicit least-squares development and applicable on arbitrary grids. The resulting linear system of algebraic equations is block tridiagonal, which permits an efficient, direct (i.e., non-iterative) solution.

In previous work unsteady solutions were obtained on a rectilinear-type, non-orthogonal, body-fitted, and periodic grid (termed "the cascade mesh") for cascades of sharp-edged airfoils aligned with the steady flow. Under the present effort the solution procedure has been extended to treat blades with rounded or blunt edges at incidence relative to the inlet flow. As part of this effort analytical studies have been conducted to clarify the behavior of first-order perturbation solutions in the vicinity of blade edges. Further, the numerical approximation has been applied to determine unsteady solutions for blunt leading-edge blades on the cascade mesh and on a dense "local" mesh surrounding the leading edge.

Numerical results are presented to illustrate the influence of blade geometry (including leading edge curvature), inlet Mach number, and inlet flow angle on unsteady response. Cascade and local mesh solutions indicate that leading edge curvature effects must be taken into account to accurately predict unsteady force and moment components in-phase with blade displacement. Predictions for staggered and unstaggered cascades of NACA 0012 and flat plate airfoils reveal that unsteady aerodynamic response is strongly dependent on blade thickness and inlet Mach number. In particular, present results indicate that the torsional stability margin for staggered cascades is substantially less for NACA 0012 than for flat plate blades. Further, the stability of out-of-phase bending or torsional motions is enhanced with increasing inlet Mach number. For subsonic attached flow, inlet flow angle or mean incidence variations appear to have only a minimal effect on unsteady force and moment. However, inlet flow angle variations do cause substantial changes in unsteady pressure distributions near blade leading edges.

INTRODUCTION

A research program is being conducted to develop an aerodynamic analysis for predicting unsteady subsonic or transonic flow in a compressor or turbine blade passage. This analysis is intended to eventually serve as the aerodynamic component of a flutter or resonant stress design prediction system for turbomachinery blade rows. To date, the effort has been concentrated on the subsonic flutter or free-vibration problem, but extensions of the analysis to treat transonic flows and forced aerodynamic excitations are planned as future work.

Background

Substantial progress has been achieved on the development of semi-analytical, subsonic and supersonic, unsteady cascade solutions (e.g. Refs. 1-5). However, these are essentially based on classical linear aerodynamic theory in which the unsteady flow is treated as a small disturbance about uniform steady flow. Such solutions do not apply if velocity gradients due to incidence, blade shape, or operation in the transonic Mach number regime are significant. Hence, they fail to meet the needs of turbomachinery designers over a wide range of practical operating conditions.

To partially overcome the foregoing limitations an aerodynamic model has been formulated for subsonic inlet and exit conditions which includes the effects of blade geometry and flow turning on unsteady response (Refs. 6, 7). Here, the unsteady flow is considered as a small-amplitude, harmonic fluctuation about nonuniform steady flow. An asymptotic expansion of the time-dependent velocity potential then provides equations which govern the steady and small-disturbance unsteady flows in a single, extended, blade-passage region of the cascade. The steady flow is determined as a solution of the full-potential equation and the unsteady flow is governed by linear equations with variable coefficients which depend on the steady flow. Key features of this formulation which permit efficient numerical prediction of unsteady forces and moments are as follows: the unsteady boundary value problem is linear and time-independent; boundary conditions are applied at the mean position of blade and wake surfaces; the unsteady flow is periodic from blade to blade; and near-field numerical solutions are matched to far-field analytical solutions. Thus a numerical approximation is only required over a single blade-passage region of finite extent.

Numerical solutions of the nonlinear steady problem are currently available for subsonic (Ref. 8) and transonic (Refs. 9, 10) flows. A numerical model for solving the unsteady equations on a rectilinear-type mesh which spans the extended blade passage region, but is not sufficiently detailed to permit an accurate resolution of the flow in the vicinity of blunt leading or trailing edges, has been developed as part of the present research program (Ref. 11). Unsteady

equations are solved on a nonorthogonal, body-fitted, and periodic mesh (herein called the cascade mesh) which facilitates the implementation of blade, wake and cascade-periodicity conditions, but disallows the use of standard difference approximations. Instead difference approximations are based on an implicit least-squares development applicable on arbitrary grids. This permits flexibility in the choice of difference neighbors and the simultaneous approximation of differential equation and boundary condition at boundary points, strategies which can significantly improve numerical accuracy.

Unsteady response predictions based on the foregoing aerodynamic and numerical models have been reported (Refs. 7, 11) for subsonic cascades of sharp-edged blades with mean camber lines aligned with the steady flow. Response predictions for flat-plate cascades are in very good agreement with those based on Smith's analytical solution (Ref. 2) for both subresonant and superresonant blade motions (Ref. 7). Predictions for unstaggered cascades consisting of double-circular-arc or thin-circular-arc profiles reveal that blade thickness produces significant coupling between the steady and unsteady flows while steady blade loading (or flow turning) due solely to blade camber causes only weak steady/unsteady interactions (Ref. 7). Recent results for staggered cascades of flat-plate and double-circular-arc blades (Ref. 11) indicate that the coupling between steady and unsteady flows caused by blade thickness is particularly strong at high Mach number and at low vibration frequency.

Similar linearizations with respect to a nonuniform steady flow have been considered in Refs. 12-16. Guiraud-Vallee, et. al. (Ref. 12) have studied compressible flow past an oscillating airfoil in a channel and have presented numerical results for subsonic and transonic flows past double-circular-arc and NACA 63A015 airfoils. Atassi and Akai (Refs. 13, 14) have derived analytic solutions for incompressible flow past a cascade of Joukowski airfoils. They have presented extensive results which indicate that blade thickness and incidence have a significant impact on unsteady response. Whitehead and Grant (Ref. 15) have developed finite-element steady and unsteady solution algorithms for subsonic cascade flows and have determined results for unsteady moments on a turbine cascade which are in agreement with experiment. Finally, Ni and Sisto (Ref. 16) regard the fluid properties as dependent variables and employ an explicit time-marching numerical procedure to determine solutions to the Euler equations of motion. This approach requires substantial computing time, but it is applicable to transonic cascade flows with strong shocks.

Scope of the Present Effort

It has been clear from previous work that improvements in the unsteady numerical approximation would be required before a practically useful flutter prediction scheme could be realized. Of most immediate concern was the development of solution procedures for general blade profiles (i.e., rounded or blunt-edged blades) and the effects of mean flow incidence. Thus under the current phase of the

overall research program, a numerical approximation based on concepts from singular perturbation theory (Ref. 17) has been adopted for resolving the unsteady boundary value problem. Unsteady equations are first solved on the "rectilinear" cascade mesh to obtain an "outer" approximation to the linear unsteady flow, and then solutions are determined on dense local meshes to obtain "inner" approximations in limited regions of high velocity gradient. The solution on the cascade mesh provides outer boundary condition data for the subsequent local solutions.

This procedure is applied here to determine the unsteady flow past cascades of blunt leading-edged airfoils. The unsteady numerical approximation on the cascade mesh has been modified so that errors caused by an inaccurate resolution of the flow near a blunt leading edge are confined to a limited region containing the leading edge. In particular, mesh points are not placed "too close" to the leading edge, and steady flow gradients are replaced by outer approximations in the vicinity of the leading edge. In addition, solutions on a dense local mesh which conforms to the shape of the airfoil and surrounds the leading edge are obtained using the implicit, least-squares, numerical approximation previously developed for the cascade mesh calculation. Unsteady response predictions for cascades of vibrating NACA 0012 and flat plate airfoils are presented to demonstrate the solution procedure and to investigate the effects of compressibility, blade geometry and mean incidence on unsteady response.

As a part of the current effort an analytical study has been conducted for the limiting case of quasi-steady, imcompressible flow to gain a better understanding of the impact of leading and trailing edge geometry on the behavior of a first-order perturbation solution. Results of this study are described in detail in the APPENDIX to this report. They indicate, that for a blunt-edge airfoil, the asymptotic series used in the present aerodynamic model will converge to the exact solution for the flow, if the airfoil displacement is sufficiently small. Further, the first-order term of the asymptotic series will be analytic throughout the flow, and is thus susceptible to a numerical resolution, provided that a sufficiently dense mesh is employed in the vicinity of a blunt leading or trailing edge.

THE UNSTEADY AERODYNAMIC MODEL

Basic equations which describe the flow past a finite-deflection cascade of airfoils undergoing small amplitude, harmonic vibrations are presented below. These equations apply to subsonic or transonic flows; i.e., flows with subsonic inlet and exit velocities, but with embedded supersonic regions adjacent to blade surfaces. The derivation essentially involves a perturbation expansion of the velocity potential which provides a nonlinear boundary value problem for the zeroth order or steady flow potential and a linear, variable-coefficient boundary value problem for the first order or unsteady potential. In the following discussion all quantities are dimensionless. Lengths have been scaled with respect to blade chord, time with respect to the ratio of blade chord to upstream free-stream speed, and pressure with respect to the upstream free-stream dynamic pressure.

Description of the Problem

Consider isentropic and irrotational flow, with negligible body forces, of a perfect gas past a two-dimensional oscillating cascade (Fig. 1). The velocity potential, $\hat{\Phi}(\vec{X}, t)$, is governed by the time-dependent, full-potential equation; i.e.,

$$\hat{A}^2\nabla^2\hat{\Phi}=\hat{\Phi}_{tt} + 2\nabla\hat{\Phi}\cdot\nabla\hat{\Phi}_t+ \nabla\hat{\Phi}\cdot\nabla(\nabla\hat{\Phi})^2/2 \tag{1}$$

The speed of sound propagation, $\hat{A}$, and the fluid pressure, $\hat{P}$, are determined from Bernoulli's equation and the isentropic relations. It follows that

$$(M_{-\infty}\hat{A})^2 = (\gamma M^2_{-\infty}\hat{P}/2)^{(\gamma-1)/\gamma} = 1-(\gamma-1)M^2_{-\infty}\left\{\hat{\Phi}_t+\left[(\nabla\hat{\Phi})^2-1\right]/2\right\} \tag{2}$$

where M is the Mach number, γ is the specific heat ratio of the fluid and the subscript $-\infty$ refers to upstream free stream conditions.

The blades of the cascade have finite thickness, camber and mean incidence angle relative to the inlet flow, and are undergoing identical, small amplitude, harmonic motions at frequency ω and constant interblade phase angle, σ. The mean or steady state positions of the blade chord lines coincide with the line segments $mG_x \le x \le 1 + mG_x$, $y = mG_y$, $m = 0, \pm 1, \pm 2, \ldots$, where G_x and G_y are the x and y - components of the cascade gap vector, $\vec{G}$, which is directed along the locus of blade leading edges with magnitude equal to the blade spacing (Fig. 1). Blade shape and orientation relative to the stream, and the amplitude and frequency of the blade motion are assumed to be such that the flow remains attached to the blade surfaces; i.e.,

$$(\nabla\hat{\Phi}\cdot\vec{n})_{\mathcal{S}_m} = \partial\vec{R}_m/\partial t\cdot\vec{n}_{\mathcal{S}_m}, \qquad m=0,\pm1,\pm2,\ldots \tag{3}$$

Here $\vec{\mathcal{R}}_m$ is a vector measuring the displacement of points on the instantaneous position of the mth blade surface, $\mathcal{S}_m$, relative to their mean positions, t is time, and $\vec{n}$ is a unit outward normal vector. In addition to Eq. (3), the fluid pressure and normal velocity must be continuous across wake surfaces, $\mathcal{W}_m$, and acoustic energy must radiate into the far field. In the inviscid approximation the wakes are represented by thin vortex sheets, each of which, emanates from a point in the vicinity of a blade trailing edge and extends downstream.

To first order the relative displacement vector for the mth blade is given by

$$\vec{\mathcal{R}}_m = \vec{r}\, e^{i(\omega t + m\sigma)} = (\vec{h} + \vec{\alpha} \times \vec{R}_p)\, e^{i(\omega t + m\sigma)} \tag{4}$$

where $\vec{h}$ defines the amplitude and direction of blade translations, α defines the amplitude of blade rotations, and $\vec{R}_p$ is a vector extending from the mean position of the mth axis of rotation (i.e., $X_p + mG_x$, $Y_p + mG_y$) to points on the mean position of the mth blade surface, S_m. Only rigid motions are considered; however, the formulation could be readily extended to include elastic deformations of the blades. The components h_x, h_y, and α of the vectors h and α are, in general, complex to permit phase differences between the translations in the x and y-directions and the rotation. These rigid two-dimensional motions describe chordwise, bending, and torsional vibrations of actual rotor blades.

Perturbation Procedure

A perturbation approach serves to replace the nonlinear, time-dependent boundary value problem for the velocity potential, $\hat{\Phi}(\vec{X}, t)$, by two time-independent boundary value problems for a zeroth order or steady potential, $\Phi(\vec{X})$, and a first order or unsteady potential, $\phi(\vec{X})\, e^{i\omega t}$. In addition, unsteady boundary conditions can be applied at the mean positions of the blade and wake surfaces, and blade pressure distributions and aerodynamic response coefficients can be evaluated in terms of information prescribed at blade mean positions. The velocity potential is expanded in an asymptotic series in ε; i.e.,

$$\hat{\Phi}(\vec{X},t) = \sum_{j=0}^{\infty} \epsilon^j \phi_j(\vec{X},t) = \Phi(\vec{X}) + \phi(\vec{X})\, e^{i\omega t} + O(\epsilon^2) \tag{5}$$

where $\vec{X}$ is the position vector and ε is a small parameter related to the amplitude of the blade motion. In addition, Taylor series expansions; e.g.,

$$\nabla\hat{\Phi}\big|_{\mathcal{S}_m} = \nabla\hat{\Phi}\big|_{S_m} + (\vec{\mathcal{R}}_m \cdot \nabla)\nabla\hat{\Phi}\big|_{S_m} + O(\epsilon^2) \tag{6}$$

are applied to refer boundary conditions to the mean positions of the blade and wake surfaces. The mean positions, W_m, of the unsteady wakes are assumed to coincide with the steady flow stagnation streamlines. After substituting the foregoing series into the full governing equations, equating terms with like powers in ε, and neglecting terms of second and higher order in ε, nonlinear and linear variable-coefficient boundary value problems are obtained, respectively for the zeroth and first order potentials.

As $\varepsilon \to 0$ the blade and wake surfaces collapse to their mean positions. Hence, the zeroth order term in the power series expansion, Eq. (5), is the velocity potential, $\Phi(\vec{X})$, due to steady flow past a stationary cascade. The cascade geometry, the prescribed form of the blade motion, and the linearity of the first order equations, require that the first order or unsteady potential be harmonic in time (i.e., $\varepsilon\Phi_1(\vec{X}, t) = \phi(\vec{X})\, e^{i\omega t}$), and that the steady and first order unsteady flows exhibit blade-to-blade periodicity; i.e.,

$$\left.\begin{aligned} \Phi(\vec{x}) &= \Phi(\vec{x}+m\vec{G}) - m\vec{V}_{-\infty}\cdot\vec{G} \\ \phi(\vec{x}) &= \phi(\vec{x}+m\vec{G})\, e^{-im\sigma} \end{aligned}\right\} \quad m = 0, \pm 1, \pm 2, \ldots \tag{7}$$

The periodicity conditions permit numerical solutions for the steady and unsteady flows to be determined in a single, extended, blade-passage region of the cascade (e.g., the region $\mathcal{D}$ in Fig. 2). Equations governing the steady potential, assumed to be known in the present study (Refs. 8-10), follow from the differential equation, Eq. (1), Bernoulli's equation, Eq. (2), and the flow tangency condition, Eq. (3), after replacing $\hat{\Phi}(\vec{X},t)$ by $\Phi(\vec{X})$ and omitting time derivative terms. Steady subsonic velocities are assumed to be approximately uniform beyond some finite distance from the blade row (e.g., $\xi<\xi_-$ or $\xi>\xi_+$ in Fig. 2); i.e.,

$$\nabla\Phi = \vec{V}_{\mp\infty} + O(\epsilon_S), \qquad \mp\xi > |\xi_\mp| \tag{8}$$

The Unsteady Boundary Value Problem

It follows from Eqs. (1), (2), and (5) that the unsteady potential is governed by a linear differential equation of the form

$$A^2\nabla^2\phi = \frac{D_S^2\phi}{Dt^2} + (\gamma-1)\nabla^2\Phi\,\frac{D_S\phi}{Dt} + \nabla\left[\frac{\nabla\Phi\cdot\nabla\Phi}{2}\right]\cdot\nabla\phi \tag{9}$$

$$\frac{D_S}{Dt} = \frac{\partial}{\partial t} + \nabla\Phi\cdot\nabla = i\omega + \nabla\Phi\cdot\nabla \tag{10}$$

and A is the local speed of sound in the steady flow. The influence of blade shape and steady turning appears in this equation through the variable coefficients (A^2, $(\gamma-1)\nabla^2\Phi$, etc.) which depend on spatial derivatives of the steady potential. Upon substituting the series expansions, Eqs. (5) and (6), into the flow tangency relation, Eq. (3), and noting the $\vec{n}_S = n_S + (\vec{\alpha}\times\vec{n}_S)e^{i\omega t} + O(\varepsilon^2)$, it follows after some algebra that the first order flow tangency condition has the form

$$\nabla\phi\cdot\vec{n} = \left[i\omega\vec{r} + \vec{\alpha}\times\nabla\Phi - (\vec{r}\cdot\nabla)\nabla\Phi\right]\cdot\vec{n}e^{im\sigma} = \left[i\omega\vec{r} - \nabla(\vec{r}\cdot\nabla\Phi)\right]\cdot\vec{n}e^{im\sigma} \tag{11}$$
$$\text{on } S_m, \quad m = 0, \pm 1, \pm 2, \ldots$$

The first term on the right-hand-side of Eq. (11) is the surface velocity. The second term accounts for the effects of blade rotation relative to the mean flow and motion through a varying mean velocity field. The conditions of continuity of pressure and normal velocity across blade wakes and the blade-to-blade periodicity of the unsteady flow require that

$$\left.\begin{aligned}\Delta_m\left(\frac{D_S\phi}{Dt}\right) &= 0\\ \Delta_m(\nabla\phi\cdot\vec{n}) &= 0\end{aligned}\right\} \quad \text{on } W_m, m = 0, \pm 1, \pm 2, \ldots \tag{12}$$

where $\Delta_m\phi$ denotes a difference across the mth wake; e.g.,

$$\Delta_m\phi = \phi(\vec{x}^-) - \phi(\vec{x}^+) = \phi(\vec{x}^- + \vec{G})e^{-i\sigma} - \phi(\vec{x}^+), \quad \vec{x} \text{ on } W_m \tag{13}$$

The unsteady potential in the reference extended passage (i.e., the region bounded by the upper and lower surfaces of the zeroth and first blade, respectively, periodic lines upstream of the blade row, and by the zeroth and first steady flow stagnation streamlines downstream of the blade row (Fig. 2)) is determined as a solution of the variable coefficient differential equation, Eq. (9), subject to the flow tangency requirement, Eq. (11), at the upper, S_0^+, and lower, S_1^-, surfaces of the zeroth and first blades, and the continuity conditions, Eq. (13), across the zeroth wake, W_0. The unsteady velocity is continuous and differentiable upstream of the blade row, and hence, the blade-to-blade periodicity condition, Eq. (7), is used in conjunction with the unsteady differential equation to determine values of the unsteady potential along upstream periodic boundaries.

Unsteady Far-Field Solutions

To complete the specification of the unsteady boundary value problem conditions at upstream and downstream boundaries of the extended blade passage region must be established. In general, unsteady disturbances do not attenuate in the far-field of the cascade, and hence, it is difficult to place explicit conditions on the unsteady potential, ϕ, at upstream and downstream boundaries of the extended blade passage region. Instead, analytic far-field solutions, based on the uniform steady velocity approximation, Eq. (8), have been determined for subsonic inlet and exit conditions. These solutions can be matched to the near field numerical solutions at finite distances upstream and downstream of the blade row (e.g., on the lines $\xi = \xi_{\mp}$ in Fig. 2).

The unsteady potential is continuous far upstream of the blade row (i.e., $\phi = \phi_c$ for $\xi < \xi_-$) and has both continuous and discontinuous components downstream of the blade row (i.e., $\phi = \phi_c + \phi_d$ for $\xi > \xi_+$). The continuous potential accounts for acoustic wave propagation into the far-field. Fourier methods can be used to provide expressions for the continuous components of the far-field potential in terms of the independent variables ξ and η where the ξ, η-coordinate axes are perpendicular and parallel, respectively, to the cascade inlet plane (Fig. 2). It follows that (cf., Refs. 6 and 7)

$$\phi_c(\xi,\eta) = \sum_{j=-\infty}^{\infty} b_{j,\mp} \exp(iq_j\eta) \exp\left[\chi_{j,\mp}(\xi-\xi_{\mp})\right], \quad \mp\xi \geq |\xi_{\mp}| \tag{14}$$

where the coefficients, $b_{j,\mp}$, are obtained from the relation

$$b_{j,\mp} = G^{-1}\int_{\eta}^{\eta+G} \phi_c(\xi,\eta)\exp(-iq_j\eta)\,d\eta, \quad \xi=\xi_{\mp} \tag{15}$$

The discontinuous component of the unsteady potential far downstream results from the counter vorticity shed from the trailing edges of the blades and convected along the blade wakes. A closed form solution (Refs. 6, 7) for this potential has been determined; i.e.,

$$\phi_d(\tau,\upsilon) = \Delta\phi(\xi_+,\eta_+)\, F(\upsilon)\exp(-i\omega\tau/V_\infty), \quad \xi \geq \xi_+ \tag{16}$$

in terms of the Cartesian coordinates τ and υ, with the τ-axis coinciding with the far-downstream, zeroth wake (Fig. 2). The constants q_j, $\chi_{j,\mp}$ and the function $F(\upsilon)$ in the foregoing equations are defined explicity in Ref. 7.

Aerodynamic Response Coefficients

Solutions to the steady and unsteady boundary value problems are required to determine blade pressure distributions and aerodynamic force and moment coefficients. The pressure at the mth blade surface is given by (c.f. Eq. (7))

$$\hat{P}_{\mathcal{S}_m} = P_S + p_{\mathcal{S}} e^{i(\omega t + m\sigma)} + \mathcal{O}(\epsilon^2), \quad m = 0, \pm 1, \pm 2 \tag{17}$$

where P and $pe^{i\omega t}$ are the zeroth (steady) and first (unsteady) order components of the fluid pressure, and $\mathcal{S}$ and S denote the moving and mean reference blade surfaces respectively. After expanding the velocity potential, $\hat{\Phi}(\vec{X}, t)$, in the manner indicated by Eqs. (5) and (6) and substituting the result along with Eq. (17) into Bernoulli's equation Eq. (2), it follows that

$$P_S = 2(\gamma M_{-\infty}^2)^{-1} (M_{-\infty} A)_S^{2\gamma/(\gamma-1)} \tag{18}$$

and

$$p_{\mathcal{S}} = \left[-2(M_{-\infty} A)^{2/(\gamma-1)} \frac{D_S \phi}{Dt} + (\vec{r} \cdot \nabla) P \right]_S \tag{19}$$

Thus the steady and unsteady components of the pressure acting on a moving blade surface, $\mathcal{S}_m$, are evaluated in terms of information supplied at the mean position of the reference blade, S. The first term on the right-hand-side of Eq. (19) is the unsteady pressure at the mean position of the blade and the second is due to motion through a varying steady pressure field. The force and moment coefficients acting on the mth blade, i.e.

$$\hat{\vec{C}}_{F_m} = \vec{C}_F + \vec{c}_F e^{i(\omega t + m\sigma)} + \mathcal{O}(\epsilon^2), \qquad m = 0, \pm 1, \pm 2, \ldots \tag{20}$$

and

$$\hat{C}_{M_m} = C_M + c_M e^{i(\omega t + m\sigma)} + \mathcal{O}(\epsilon^2), \quad m = 0, \pm 1, \pm 2, \ldots \tag{21}$$

are determined by simple integrations over the mean position of the reference blade. After some algebra it follows that the steady, $\vec{C}_F$ and C_M, and unsteady $\vec{c}_F$ and c_M, force and moment coefficients are given by

$$\vec{C}_F = -\oint_S P_S \vec{n}\, ds, \qquad C_M = \oint_S P_S \vec{R}_p \cdot d\vec{s} \tag{22}$$

$$\vec{C}_F = -\oint_S p_s \vec{n}\, ds + \vec{\alpha} \times \vec{C}_F, \qquad C_M = \oint_S p_s \vec{R}_p \cdot d\vec{s} \tag{23}$$

where $d\vec{s}$ is a differential vector tangent to the mean blade surface. It should be noted that the moment is taken about the moving pitching axis. The unsteady force and moment coefficients are the important results of an aerodynamic analysis intended for flutter predictions. Knowledge of these coefficients permits the evaluation of aerodynamic work per cycle and/or aerodynamic damping (Ref. 18) either of which can be used to determine whether the airstream supports or suppresses a prescribed blade motion.

THE UNSTEADY NUMERICAL MODEL

In the approximate representation of a physical problem by a discrete numerical model, several components must be constructed. For the present case, these components include the discrete domain (or calculation mesh), the approximating algebraic equations, and the solution procedure. Such components are generally not independent of each other with the choice of one influencing the choice of another. For instance, if the algebraic system is linear with proper structure, a direct solution procedure may be used, but if the system is nonlinear or linear but large and without particular structure an iterative technique may be necessary. It is important that the choice of one component not place overly restrictive constraints on the other components.

Calculation Meshes

Flow about a blunt edged airfoil has two length scales associated with it. The effects of airfoil geometry and motion on the undisturbed stream generally scale with blade chord and can be modeled on a calculation mesh of moderate density. However, flow phenomena near a blunt edge scale with edge radius and can be accurately modeled only on a much finer mesh. In this study, which involves flow through a cascade of airfoils with blunt leading edges and pointed trailing edges, the large scale effects of airfoil geometry and motion and their resulting flow are termed "cascade" while the small scale effects of the blunt leading edge and their resulting flow are termed "local". It would be difficult to approximate accurately and efficiently on a single mesh both the cascade and local effects because of the different length scales involved. Instead, in this study, the cascade flow is modeled on a cascade mesh of moderate density and the local flow is modeled on a local mesh of high density.

The definition of an appropriate cascade mesh is much more difficult than the definition of an isolated airfoil mesh. For the latter there are easily defined orthogonal meshes, e.g., potential-streamline meshes, "polar" meshes composed of normal and circumferential lines, and "parabolic" combinations. For a cascade these meshes are not so easily employed. For instance, the potential-streamline mesh is not periodic since potential lines generally are not parallel to the cascade. Boundary conditions arising from cascade periodicity - in this case the periodic and wake boundary conditions of Eqs. (7,12) - can be approximated on such a mesh only with difficulty, since the mismatch of the mesh across the periodic boundary will require some sort of interpolation. Furthermore, the resulting linear system will not be tightly banded precluding the use of direct solution techniques. Orthogonal "polar" type meshes can be defined using conformal mapping as in Ref. 9. However, the necessary mappings

are not presently known for all cascades particularly those with high turnings or small gap to chord ratios. In contrast, the definition of an appropriate local mesh depends only on airfoil geometry and so is independent of whether the airfoil is isolated or placed in a cascade.

The cascade mesh used in this study is the periodic and body fitted but nonorthogonal one shown schematically in Fig. 3. It is composed of "axial" lines, which are parallel to the blade row making the mesh periodic, and "tangential" curves, which are percentile averages of the upper and lower boundaries making the mesh body fitted. The leading and trailing edge axial lines are not in the cascade mesh eliminating the need for special considerations at leading and trailing edge points. The local mesh is the "polar" mesh shown schematically in Fig. 4. It is composed of "radial" lines normal to the airfoil surface and "circumferential" lines which roughly parallel the airfoil surface.

Two Step Calculation Procedure

The unsteady boundary value problem of Eqs. (9-16) is modeled on the cascade mesh using the algebraic approximations described below. In order to remove local phenomena induced by a blunt leading edge from the cascade solution, steady potential derivatives are modified to remove leading edge curvature effects. This results in a cascade solution which is akin to an "outer" solution. These leading edge effects are then restored to the solution calculated on the local mesh with unmodified steady potential derivatives. Cascade effects are introduced to the local solution by interpolating the potential calculated on the cascade mesh to the outer radial and circumferential boundaries of the local mesh and imposing the interpolated potential distribution as a boundary condition. The solution to the unsteady boundary value problem is then taken to be the local solution in the local mesh region and the cascade solution elsewhere.

To date, the cascade and local flows have been calculated by the two-step procedure described above, in which the local solution is essentially a correction to the cascade solution near the leading edge. Because the local leading edge effects are not in the cascade calculation, it is necessary to choose the local region extensive enough so that leading edge effects become insignificant on the local mesh boundaries. This insures that the local boundary value problem has valid information on the outer boundary. It is planned eventually to iterate between cascade and local solutions until the two solutions balance at the interface. When this is done a much smaller local region will suffice.

Algebraic Approximations

The nonorthogonality of the cascade mesh precludes the use of Cartesian difference approximations based on Taylor series expansions and so requires the development of more general approximations. These approximations are then used in both the

cascade and local problems. Consider a linear differential operator, $\mathcal{L}$, which operates on a constant by multiplying that constant by q^0. $\mathcal{L}\phi$ is to be approximated at the mesh point Q_0 in terms of the values of ϕ at Q_0 and at certain neighboring mesh points, $Q_1, \ldots, Q_M$, which, with Q_0, are called a neighbor set. Quantities subscripted with 0 or m are evaluated at the corresponding neighbor set member. The approximation is developed in terms of an implicit interpolation of the form

$$\delta\phi \equiv \phi - \phi_0 \approx F = \sum_{n=1}^{N} \gamma^n f^n \equiv \underset{\sim}{f}^T \underset{\sim}{\gamma} \tag{24}$$

where the f^n are prescribed interpolating functions which vanish at Q_0 - homogeneous polynomials, for instance - and the γ^n are interpolating coefficients, which must be determined. The definition of γ depends on the specific interpolation used, but, in any case, it is assumed to depend on values of ϕ at Q_0 and its neighbors; i.e.,

$$\underset{\sim}{\gamma} = \mathcal{C}\,\underset{\sim}{\delta\phi} + \underset{\sim}{c}^0 \phi_0 + \underset{\sim}{c}^I \tag{25}$$

where $\underset{\sim}{\delta\phi} = (\delta\phi_1, \ldots, \delta\phi_M)^T$, and the interpolating matrix, $\mathcal{C}$, and vectors, $\underset{\sim}{c}^0$ and $\underset{\sim}{c}^I$, depend on the geometry of the neighbor set but are independent of ϕ. In the present analysis the interpolation arises from a least squares fit, described below, and thus the method is termed an implicit least squares approximation. After replacing $\delta\phi$ by its interpolate, it follows that

$$(\mathcal{L}\phi)_0 \approx \mathcal{L}(\phi_0 + F)_0 = q^0\phi_0 + (\underset{\sim}{\mathcal{L}f})_0^T \underset{\sim}{\gamma} \tag{26}$$

where $\underset{\sim}{\mathcal{L}f}$ is the Nx1 vector with components $\mathcal{L}f^n$. Further, after combining Eqs. (25) and (26), the differential expression $\mathcal{L}\phi$ is approximated by the difference expression

$$(\mathcal{L}\phi)_0 \approx (L\phi)_0 \equiv \sum_{m=1}^{M} \beta_m \phi_m + \beta_0\phi_0 + \beta_I \tag{27}$$

where L is the difference operator derived from $\mathcal{L}$ and the coefficients of the difference operator are given by

$$\begin{aligned} \underset{\sim}{\beta}^T &= (\underset{\sim}{\mathcal{L}f})_0^T \mathcal{C} \\ \beta_0 &= (\underset{\sim}{\mathcal{L}f})_0^T \underset{\sim}{c}^0 - \sum_{m=1}^{M} \beta_m + q^0 \\ \beta_I &= (\underset{\sim}{\mathcal{L}f})_0^T \underset{\sim}{c}^I \end{aligned} \tag{28}$$

$\underset{\sim}{\beta}$ being the Mx1 vector with components β_m.

Since the differential operator $\mathcal{L}$ has no inhomogeneous term, $(L\phi)_0$ might be expected to have the form

$$(L\phi)_0 = \sum_{m=1}^{M} \beta_m (\phi_m - \phi_0) + q^0 \phi_0 \qquad (29)$$

which emphasizes the "difference" aspect of its definition. Equations (27) and (29) would be equivalent if the vectors $\underset{\sim}{c}^0$ and $\underset{\sim}{c}^I$ were zero. Although this is the case for most interpolations, $\underset{\sim}{c}^0$ and $\underset{\sim}{c}^I$ are nontrivial if the interpolate F is constrained, as it may be at a boundary where ϕ satisfies both a boundary condition (which is defined by the operator $\mathcal{L}$) and the field equation (which becomes the constraint). Thus at a boundary, both the field equation and boundary condition can, in effect, be simultaneously approximated - a powerful feature of the implicit least squares approximation.

Least Squares Difference Approximation

The difference operator, L, which approximates the differential operator $\mathcal{L}$ is defined by Eqs. (27, 28) once the interpolation matrix and vectors are determined. First the interpolating functions, f^n, of Eq. (24) must be chosen. Common choices are the polynomials

$$N=5: \quad f^1=\delta\xi, \quad f^2=\delta\eta, \quad f^3=\delta\xi^2, \quad f^4=\delta\xi\cdot\delta\eta, \quad f^5=\delta\eta^2 \qquad (30)$$

where $\delta\xi = \xi - \xi_0, \delta\xi^2 = (\xi-\xi_0)^2$, etc. Here, ξ and η could be any convenient coordinates but in this study, are taken to be the cascade axial and tangential coordinates indicated in Fig. 2. The interpolation coefficients must then be defined. With eight neighbors but only five interpolating functions, it is impossible to define $\underset{\sim}{\gamma}$ such that F implicitly agrees with $\delta\phi$ at all neighbors. On a rectangular mesh the reasonable but ad hoc decisions that F agree with $\delta\phi$ at the neighbors above, below, right and left and that a certain combination of F values at the corner neighbors agree with the same combination of $\delta\phi$ values leads to an interpolation matrix which produces the familiar difference coefficients obtained by Taylor series expansions. On a general mesh these ad hoc decisions are no longer reasonable. What is needed is a formal method of defining the interpolating coefficients from the available data regardless of the geometry of the neighbor set. Least squares techniques provide such a method.

A measure of the error in replacing $\delta\phi$ with its interpolate, F, in Eq. (24) is

$$e(\underset{\sim}{\gamma}) \equiv \sum_{m=1}^{M} w_m \Big[\sum_{n=1}^{N} \gamma^n f_m^n - \delta\phi_m \Big] \overline{\Big[\sum_{n=1}^{N} \gamma^n f_m^n - \delta\phi_m \Big]} \tag{31}$$

where the over bar indicates complex conjugation and the w_m are chosen to give proper importance to the various neighbors. In practice w_m is usually given by

$$w_m = 1/|Q_m - Q_0| \tag{32}$$

but it may be set to zero if the corresponding neighbor is to have no influence. The real, nonnegative function e is minimized as a function of the real and imaginary parts of $\underset{\sim}{\gamma}$. There results the following complex linear system to determine $\underset{\sim}{\gamma}$:

$$\mathcal{A}\underset{\sim}{\gamma} = \mathcal{B}\delta\underset{\sim}{\phi} \tag{33}$$

The NxN matrix $\mathcal{A}$ and NxM matrix $\mathcal{B}$ are given in terms of the MxN matrix, $\mathcal{F} = (f_m^n) = (f^n(Q_m))$ and the MxM diagonal matrix, W = diag $(w_1, \ldots, w_m)$ by

$$\begin{aligned} \mathcal{A} &= \mathcal{F}^* W \mathcal{F} \\ \mathcal{B} &= \mathcal{F}^* W \end{aligned} \tag{34}$$

where the superscript * indicates conjugate transposition. The interpolation matrix is then given by

$$\mathcal{C} = \mathcal{A}^{-1}\mathcal{B} \tag{35}$$

and the interpolation vectors are zero.

At a boundary point, Q_0, the operator, $\mathcal{L}$, to be approximated usually is derived from a boundary condition rather than from the field equation, which probably also holds at Q_0. Suppose the field equation, Eq. (9), is generalized to have the form

$$\mathcal{M}\phi = h^I \tag{36}$$

where $\mathcal{H}$ is a linear differential operator which operates on a constant by multiplying the constant by h^0. Approximate $\mathcal{H}\phi$ by $\mathcal{H}(\phi_0 + F)$ and apply at Q_0 to obtain

$$g(\underset{\sim}{\gamma}) \equiv (\underset{\sim}{\mathcal{H}f})_0^T \underset{\sim}{\gamma} + h^0\phi_0 - h^I = 0 \tag{37}$$

where $g(\gamma)$ is a complex constraint functional and $\underset{\sim}{\mathcal{H}f}$ has components $\mathcal{H}f^n$. Equation (37) describes an algebraic constraint on the interpolate, F. The coefficient vector, $\underset{\sim}{\gamma}$, is then determined by minimizing the error function, e, subject to this constraint. This is accomplished by using a complex Lagrange multiplier and minimizing the constrained error function

$$e_c(\underset{\sim}{\gamma},\lambda) \equiv e(\underset{\sim}{\gamma}) + \mathrm{Re}\{\lambda\}\,\mathrm{Re}\{g(\underset{\sim}{\gamma})\} + \mathrm{Im}\{\lambda\}\,\mathrm{Im}\{g(\underset{\sim}{\gamma})\} \tag{38}$$

with respect to the real and imaginary parts of $\underset{\sim}{\gamma}$ and the Lagrange multiplier, λ. Equation (33) becomes

$$\begin{aligned} \mathcal{A}\,\underset{\sim}{\gamma} + (\overline{\underset{\sim}{\mathcal{H}f}})_0\,\lambda &= \mathcal{B}\,\underset{\sim}{\delta\phi} \\ (\underset{\sim}{\mathcal{H}f})_0^T\,\underset{\sim}{\gamma} &= h^I - h^0\phi_0 \end{aligned} \tag{39}$$

The interpolation matrix and vectors are then given by

$$\begin{aligned} \mathcal{C} &= \left[\mathcal{I} - \frac{1}{H}\,\mathcal{A}^{-1}(\overline{\underset{\sim}{\mathcal{H}f}})_0(\underset{\sim}{\mathcal{H}f})_0^T\right]\mathcal{A}^{-1}\mathcal{B} \\ \underset{\sim}{c_0} &= -\frac{h^0}{H}\,\mathcal{A}^{-1}(\overline{\underset{\sim}{\mathcal{H}f}})_0 \\ \underset{\sim}{c_I} &= \frac{h^I}{H}\,\mathcal{A}^{-1}(\overline{\underset{\sim}{\mathcal{H}f}})_0 \end{aligned} \tag{40}$$

where H is the scalar

$$H = (\underset{\sim}{\mathcal{H}f})_0^T\,\mathcal{A}^{-1}(\overline{\underset{\sim}{\mathcal{H}f}})_0 \tag{41}$$

Let s be the scalar

$$s = \frac{1}{H}(\underset{\sim}{\mathcal{L}f})_0^T\,\mathcal{A}^{-1}(\overline{\underset{\sim}{\mathcal{H}f}})_0 \tag{42}$$

Then, from Eq. (28)

$$\underset{\sim}{\beta}^T = \left[(\underset{\sim}{\mathcal{L}f})_0^T - s(\underset{\sim}{\mathcal{H}f})_0^T\right]\mathcal{A}^{-1}\mathcal{B} \tag{43}$$

Thus β is defined as if the operator $\mathcal{L} - s\mathcal{H}$ were being approximated; i.e., the operator being constrained is a particular linear combination of the boundary condition operator and the constraint operator.

Solution Procedure

For the cascade calculation, the neighbor sets are generally defined as shown in Fig. 3; i.e., "centered" neighbor sets are defined if Q_0 is a field point, and "one-sided" neighbor sets are defined if Q_0 lies on a blade or wake boundary. In any case, all neighbors fall on the axial mesh line through Q_0 and on the two immediately adjacent axial lines. This placement is important to obtain a desirable structure for the solution matrix. Derivatives of the unsteady potential exhibit singular behavior at sharp edges, in that $\phi \sim \mathcal{O}(r_E^{1/2})$ near leading edges and $\phi \sim \mathcal{O}(r_E^{3/2})$ near trailing edges where r_E denotes distance from the edge (Ref. 19). Rapid, near-singular, variations are also observed near blunt edges. Thus for cascade calculations, either the first point(s) on the blade or the first point off the blade on the upper and lower boundaries of the passage (Fig. 2) is deleted from neighbor sets near blade edges to ensure that differences are not taken across singularities. Affected neighbor sets are said to be adjusted.

At field points the unsteady differential equation, Eqs. (9,10), is approximated using centered neighbor sets. For points on the upstream periodic boundary (Fig. 2), ϕ values at neighbors above the mesh region are related to ϕ values at points within the mesh region by the periodic condition, Eq. (7). On the lower periodic boundary the periodic condition is directly applied, since to approximate the field equation on both upper and lower periodic boundaries would be redundant. For points on the far-upstream boundary ($\xi = \xi_-$), ϕ values at neighbors upstream of the mesh region are related to ϕ values on the boundary using the far field condition, Eq. (14), with the Fourier coefficients being evaluated using Eq. (15). The infinite sum in Eq. (14) is truncated after a few terms - usually three- in each direction, and the integral in Eq. (15) is approximated using a trapezoid rule quadrature. A similar procedure is followed on the far-downstream boundary ($\xi = \xi_+$), but here the discontinuous component of ϕ given in Eq. (16) must be taken into account. At blade points the flow tangency condition, Eq. (10), is approximated using "one-sided" neighbor sets. At wake points the pressure continuity and normal velocity conditions of Eq. (12) are also approximated using "one-sided" neighbor sets. Letting $L_{W_1^-}$ and $L_{W_0^+}$ represent either one of the approximating difference operators on the upper and lower wakes respectively, the resulting difference equations take the form

$$L_{W_1^-}\phi(Q_{W_1^-}) - e^{i\sigma} L_{W_0^+}\phi(Q_{W_0^+}) = 0 \qquad (44)$$

where $Q_{W_0^+}$ is a mesh point on the lower wake and $Q_{W_1^-}$ is the corresponding point on the upper wake. One of these (continuity of pressure) is applied on one wake boundary and the other (continuity of normal velocity) is applied on the other wake boundary. At both blade and wake points, the difference equations are constrained to satisfy the field equation.

For the local calculation matters are much simpler since no special considerations (e.g., neighbor set adjustment) need be taken at the leading edge and the many types of boundary conditions have become only two. Neighbor sets are chosen as for the global calculation, i.e., centered at field points and one-sided at boundary points. The unsteady differential equation, Eqs. (9, 10), and the flow tangency condition, Eq. (11), are approximated as above at field points and blade points respectively. At points on the outer boundary of the local mesh the unsteady potential is given the value interpolated from the cascade calculation.

Let $\underset{\sim}{\phi}_\ell$ be a vector of the ϕ values on the ℓth axial mesh line for the cascade calculation or on the ℓth radial mesh line for the local calculation. Because neighbor sets of points on the ℓth line include points only from lines $\ell-1$, ℓ, $\ell+1$, (and because the cascade calculation mesh is periodic,) the systems of linear algebraic equations for both cascade and local calculations have the following block tridiagonal form.

$$\begin{aligned} B_1 \underset{\sim}{\phi}_1 + C_1 \underset{\sim}{\phi}_2 &= \underset{\sim}{d}_1 \\ A_\ell \underset{\sim}{\phi}_{\ell-1} + B_\ell \underset{\sim}{\phi}_\ell + C_\ell \underset{\sim}{\phi}_{\ell+1} &= \underset{\sim}{d}_\ell \quad , 2 \le \ell \le L-1 \\ A_L \underset{\sim}{\phi}_{L-1} + B_L \underset{\sim}{\phi}_L &= \underset{\sim}{d}_L \end{aligned} \tag{45}$$

With this structure, the systems can be solved directly and efficiently using Gaussian elimination as described in Refs. 20 and 21. The sub-matrices A_ℓ and C_ℓ, are sparse (as is B_ℓ) being basically scalar tridiagonal. This can be taken advantage of to improve computational efficiency during the forward elimination phase of the solution (Ref. 21). If a non-periodic mesh were employed for the cascade problem, the block tridiagonal structure would be lost and an iterative procedure would be required to obtain a solution.

NUMERICAL RESULTS

The unsteady aerodynamic model accounts for the effects of blade geometry, including blunt leading and trailing edges, and mean incidence on unsteady response. However until recently, the unsteady numerical model was applied only on a rectilinear-type mesh which spanned the extended-blade-passage region (the cascade mesh shown in Fig. 3). Thus previous unsteady response predictions were restricted to cases in which the flow near blade edges could be reasonably approximated on this mesh; i.e., to cascades consisting of sharp-edged blades with mean camber lines aligned with the steady flow (Refs. 7 and 11). Predictions for flat plate cascades were shown to be in good agreement with Smith's (Ref. 2) semi-analytical results for both subresonant and superresonant blade motions. Further predictions for double-circular-arc and thin-circular-arc blade profiles revealed that blade thickness produces a strong coupling between the steady and unsteady flows, particularly at high Mach number or low vibration frequency, while steady flow turning due to blade camber causes only weak steady/unsteady interactions.

Under the present research program the numerical model has been developed further to treat cascades of blunt leading-edged airfoils at incidence relative to the inlet flow. The approximation on the cascade mesh has been modified so that errors due to an inadequate resolution of the large unsteady gradients near a blunt leading edge are confined to a limited region surrounding the leading edge. In addition, the numerical model has been applied on a dense local mesh (Fig. 4) to capture details of the rapidly varying flow in the neighborhood of a blunt leading edge. Thus for a cascade of blunt leading-edged airfoils, a numerical solution is first determined on a cascade mesh for the entire extended blade-passage domain, and then, a detailed solution is determined on a local mesh in the vicinity of the leading edge. The solution on the cascade mesh supplies boundary condition information (i.e., the unsteady potential distribution) on the outer boundary of the local mesh for the latter calculation.

Present Examples

The foregoing procedure has been applied to determine the unsteady flow past cascades of vibrating NACA 0012 airfoils. The mean position of the zeroth or reference blade surface is defined by the equation (Ref. 22)

$$y(x) = \pm 5T\left[0.2969\sqrt{x} - 0.1260x - 0.3516x^2 + 0.2843x^3 - 0.1015x^4\right], 0 \le x \le 1 \qquad (46)$$

where T = 0.12 is the blade thickness. The leading edge radius of the airfoil is $1.1019T^2 = 0.015867$. For the present application the coefficient of the x^4 term has been changed to 0.1036 so that the upper and lower surfaces close at x = 1 in a wedge-shaped trailing edge. Results have been determined for unstaggered (Θ = 0 deg.) and staggered (with Θ = 45 deg.) cascades with unit gap-chord ratio (G = 1) for prescribed steady inlet Mach numbers, $M_{-\infty}$, and flow angles, $\Omega_{-\infty}$. Corresponding exit Mach numbers, M_{∞}, and flow angles, Ω_{∞}, are determined by a global mass balance and the application of a Kutta condition, i.e.,

$$\vec{V} \cdot \vec{ds}\Big|_{s^-} = -\vec{V} \cdot \vec{ds}\Big|_{s^+} \quad , x = 1 \tag{47}$$

at blade trailing edges. Unsteady pressure difference distributions; i.e.,

$$\Delta p(x) = p_{s^-}(\vec{x}) - p_{s^+}(\vec{x}) = p_{s_1^-}(\vec{x}+\vec{G})\, e^{-i\sigma} - p_{s_0^+}(\vec{x}) \tag{48}$$

and aerodynamic response coefficients, $c_L = \vec{c}_F \cdot \vec{e}_y$ and c_M, will be presented for cascades of NACA 0012 airfoils undergoing unit-frequency (ω = 1), out-of-phase ($\sigma = \pm$ 180 deg.), single-degree-of-freedom, heaving (with h_y = (1, 0)) or pitching (with α = (1, 0)) motions about an axis at mid-chord ((X_p, Y_p) =(0.5, 0)). These rigid, two-dimensional, motions model bending or torsional vibrations of actual rotor blades. When the imaginary parts of the bending or torsional amplitudes are set equal to zero, the real and imaginary parts of the response coefficients, Δ_p, c_L, and c_M, are in-phase with the blade displacement and velocity, respectively. The stability of single-degree-of-freedom bending motions with Im $\{h_y\}$ = 0 is governed by the sign of the imaginary part of the lift coefficient. If Im $\{c_L\} < 0$ the airstream tends to suppress the motion, and hence this motion is stable according to linear theory. Similarly, if Im $\{\alpha\} = 0$, single-degree-of-freedom torsional motions are stable when Im $\{c_M\} < 0$ (Ref. 23). In addition to the NACA 0012 cases, for purposes of comparison, numerical results will be presented for oscillating flat plate cascades with blade mean positions aligned parallel to the free-stream direction. In this case Φ = x and the unsteady equations reduce to those of classical small-disturbance theory (Ref. 19).

Unsteady solutions for NACA 0012 and flat plate cascades were determined for a blade passage region extending two axial chords upstream and downstream of the blade row with far-field Fourier expansions, Eq. (14), being truncated after j = 3. For the NACA 0012 cases unsteady solutions were calculated on both cascade (Fig. 3) and local (Fig. 4) meshes. In addition, steady flows have been calculated on similar but coarser meshes using the finite area approximation developed by Caspar, Hobbs, and Davis (Ref. 8), and steady data has been defined on the unsteady meshes using constrained, polynomial, least-squares interpolations in an explicit manner. For the flat plate cases the steady flow is known and unsteady calculations are only required on the cascade mesh.

The unsteady results reported here were determined on cascade meshes consisting of 15 tangential lines and from 69 to 73 axial lines, 25 to 28 of which intersect blade surfaces. To minimize the effects of local errors on the cascade mesh solution, axial mesh lines did not intersect blade leading and trailing edges. Further, steady derivative behavior in the vicinity of a blunt leading edge was modified to depend on a position vector emanating from the leading edge rather than on a position vector emanating from the center of the leading edge circle (c.f. the APPENDIX to this report) using an extrapolation based on the Prandtl-Glauert transformation. The spacing of the axial mesh lines as a percentage of axial chord varied from 20 percent at far-field boundaries to approximately 2 percent near blade edges to 5 percent near midchord, while the spacing between the tangential mesh lines as a percentage of distance between the upper and lower, extended-passage, boundaries varied from 2 percent near the boundaries to 15 percent near the middle of the passage.

The local mesh employed for the NACA 0012 examples consisted of 12 circumferential lines which wrapped around the leading edge of the airfoil and extended from normal lines to the upper and lower surfaces at midchord, and 100 "radial" or normal lines which extended outward from the airfoil to one-half the minimum distance (i.e. the throat) between adjacent blades. The normal lines were spaced so that circumferential distances half way out (i.e., at 25 percent of the throat) were equal. The distance between circumferential lines as a percentage of the throat varied from 0.125 percent near the airfoil to 10.5 percent at the outer boundary of the local region. Once steady derivative information has been stored, unsteady solutions on the cascade and local meshes described above require approximately 30 and 20 seconds, respectively, of CPU time on a UNIVAC 1100/81 system. It appears that the cascade and local meshes, used presently, are more dense than necessary for an accurate resolution of the unsteady flow, and hence, substantial reductions in computing time should be realized in future studies.

Unstaggered Cascades

Results for unstaggered NACA 0012 and flat plate cascades are shown in Figs. 5 through 13. For the NACA 0012 cascade, inlet Mach numbers, $M_{-\infty}$, of 0.3, 0.5, and 0.6 and inlet flow angles, $\Omega_{-\infty}$, (Fig. 1) of 0 deg., 5 deg., and 10 deg. have been considered. For the flat plate cascade the inlet Mach numbers are 0.3, 0.5, 0.6, and 0.7 and the inlet flow angle is 0 deg. in each case. Cascade and local mesh solutions for unsteady pressure difference distributions near the leading edge of the reference NACA 0012 blade are shown for out-of-phase bending and torsional vibrations in Figs. 5 and 6, respectively, for $M_{-\infty} = 0.5$ and $\Omega_{-\infty} = 0$ deg. Here the pressure difference is plotted versus the square-root of the distance along the airfoil chord from the leading edge. Solutions on the cascade mesh approximate analytical singularities in Δp at the leading edge,

which are removed by the subsequent local solution. The latter determines a zero pressure difference at a blunt leading edge and local extrema in unsteady pressure difference near the leading edge. For the bending motion (Fig. 5) there is a local minimum in Re $\{\Delta p\}$ at $x \sim 0.0035$ and in Im $\{\Delta p\}$ at $x \sim 0.013$, while for the torsional motion (Fig. 6) the real and imaginary pressure differences reach local maxima at $x \sim 0.0009$ and $x \sim 0.012$, respectively, and the real component has a local minimum at $x \sim 0.03$. It should be noted that the singular behavior predicted by the cascade mesh solution for the real component of the pressure difference due to torsion (Re $\{\Delta p\} \to \infty$ as $x \to 0^+$; c.f. Fig. 6) differs from that predicted by classical linear theory (Re $\{\Delta p\} \to -\infty$ as $x \to 0^+$; c.f. Fig. 11). This difference is due to the contribution of higher order singular terms (i.e., (Re $\{p\} \sim O(x^{-3/2})$ as $x \to 0$) which appear in an "outer" approximation to the unsteady flow near a blunt leading edge. As indicated in Figs. 5 and 6, significant differences exist between the real components of the lift and moment coefficients predicted by the cascade mesh solution and the combined (i.e., cascade plus local) solution. In the latter case local mesh results apply in the region covered by the local mesh and cascade mesh results apply elsewhere. However, the cascade solution provides a good approximation to the imaginary components of the response coefficients.

The effect of inlet Mach number variation on the unsteady response to a cascade of vibrating NACA 0012 airfoils is illustrated in Figs. 7 through 9 for inlet Mach numbers of 0.3, 0.5, and 0.6. In each case the inlet flow angle is 0 deg. Steady Mach number distributions on the reference blade surface are shown in Fig. 7. For the prescribed inlet conditions surface Mach numbers reach maximum values of 0.379, 0.667, and 0.864 at $x = 0.132$, $x = 0.152$ and $x = 0.195$, respectively. Results depicted in Figs. 8 and 9 indicate that the unsteady response is strongly dependent on inlet Mach number, particularly at high Mach number. For out-of-phase bending motions (Fig. 8) the imaginary component of the unsteady pressure difference increases near the leading edge, but decreases over the remainder of the airfoil as inlet Mach number increases. This behavior results in a decrease in imaginary lift component; i.e., an increase in aerodynamic force opposing the blade motion. For out-of-phase torsional vibrations (Fig. 9), as M_∞ increases the imaginary component of the unsteady pressure difference increases substantially over the forward 40 percent of the airfoil and decreases over the remaining 60 percent resulting in an increase in the unsteady moment opposing the motion (i.e., Im $\{c_M\}$ decreases). Hence, the effect of higher inlet Mach number is stabilizing for the two motions.

Similar results are shown in Figs. 10 and 11 for flat plate cascades. Here the steady Mach number is a constant. An increase in Mach number has a stabilizing effect on the motions of a flat plate cascade, but Mach number variation has a less pronounced effect on the aerodynamic response to vibrating flat plate blades than it does for the NACA 0012 profiles. A comparison between unsteady predictions for the NACA 0012 and flat plate cascades for a given inlet Mach number reveals the important influence of blade geometry on unsteady aerodynamic response. The results provided in Figs. 8 through 11 indicate that the effect of blade thickness is stabilizing for the subsonic attached flows considered, particularly at high Mach number.

The effect of mean incidence on the response to single-degree-of-freedom motions of unstaggered NACA 0012 cascades has been examined by computing unsteady solutions for an inlet Mach number of 0.5 and inlet flow angles of 0 deg., 5 deg., and 10 deg. The numerical results indicate that an inlet flow angle variation from 0 to 10 deg. has little impact on overall unsteady pressure difference distribution, and hence, unsteady lift and moment coefficients. An increase in mean incidence angle caused significant variations in unsteady surface pressure near the leading edge of the airfoil, but produced only a slight increase in stability margin for the bending or torsional vibrations. Real and imaginary unsteady surface pressure distributions near the leading edge of the reference blade are shown in Figs. 12 and 13, respectively, for the torsional case. Although there are substantial differences in unsteady pressure in the immediate vicinity of the leading edge ($0 \leq \sqrt{x} \leq 0.2$) these do not persist over the entire airfoil, and therefore unsteady force and moment coefficients are relatively unaffected by the changes in inlet flow angle.

Staggered Cascades

Results for staggered cascades of NACA 0012 and flat plate airfoils are shown in Figs. 14 through 18 for a stagger angle of 45 deg. and inlet Mach numbers equal to 0.3, 0.5 and 0.7. The inlet flow angle is 5 deg. for the NACA 0012 and 0 deg. for the flat plate cases. Surface Mach number distributions for NACA 0012 profile are shown in Fig. 14. Peak Mach numbers on the suction surface are 0.379, 0.649, and 0.970 and occur at x = 0.053, x = 0.068, and x = 0.095, respectively. The steady flows stagnate on the lower surface of the airfoil within a distance of 0.03 percent of blade chord from the leading edge and the stagnation point moves closer to the leading edge as inlet Mach number increases. Unsteady response predictions for out-of-phase bending (Fig. 15) and torsional (Fig. 16) vibrations of the NACA 0012 profiles follow similar trends with Mach number, M_∞, as do the corresponding results for unstaggered cascades (Figs. 7 and 8). For the bending case the real component of the pressure difference distribution decreases substantially over the forward half of the airfoil leading to a reduction in real lift component and an increase in the real counterclockwise moment. The imaginary component of the pressure difference distribution increases near the leading edge, but decreases over most of the airfoil providing a substantial increase in the magnitude of the force opposing the motion and a reduction in counterclockwise moment at high Mach number. For the torsional case real pressure differences decrease over most of the blade providing a reduction in lift and an increase in counterclockwise moment. Further, imaginary pressure differences increase on the forward 30 percent of the blade and decrease over the remainder of the blade, leading to a reduction in lift and an increase in the moment opposing the motion. Hence, the effect of increasing inlet Mach number is to enhance the stability of both motions.

Results for the staggered flat plate cascades reveal a reduction in the imaginary component of the unsteady pressure difference due to bending (Fig. 17) over most of the airfoil, and hence, an increase in the unsteady force opposing the motion with increasing Mach number. Further, there is a substantial increase in Im $\{\Delta p\}$ due to torsion (Fig. 18) over the front-half of the airfoil, and hence, an increase in the moment opposing the motion, as Mach number increases. A comparison of the results given in Figs. 15 through 18 indicates that for the subsonic Mach number range considered, blade thickness enhances the aerodynamic stability of the bending motions, but causes a reduction in stability margin for the torsional motions.

Unsteady Moment Due to Torsion

In an effort to briefly examine the effect of blade geometry on overall torsional stability, limited additional calculations have been performed for the staggered($G = 1$, $\Theta = 45$ deg.) cascades of NACA 0012 and flat plate airfoils undergoing single-degree-of-freedom torsional vibrations about midchord. For these cases the inlet Mach number was set at 0.7 and the inlet flow angle was set at 5 deg. for the NACA 0012 cascade and at 0 deg. for the flat plate configuration. Results were first determined for unit frequency motions over the entire interblade phase angle range (i.e., -180 deg. $< \sigma <$ 180 deg.), and then for motions at $\omega = 0.5$ over the subresonant range of positive interblade phase angles. At unit frequency, superresonant conditions (i.e. acoustic waves persist far upstream and/or far downstream of the cascade, c.f. Ref. 7) exist for -28.6 deg. $< \sigma <$ 112.4 deg. for the NACA 0012 cascade and for -29.4 deg. $< \sigma <$ 107.3 deg. for the flat plate cascade. The results for the imaginary component of the moment coefficient are depicted in Fig. 19. For superresonant motions the aerodynamic damping (which is proportional to $-\text{Im}\{c_M\}$) is greater for the NACA 0012 than for the flat plate blades. However, this situation is dramatically reversed over most of the subresonant region. The maximum calculated values of Im $\{c_M\}$ were -0.157 at $\sigma = 120$ deg. (subresonant) for the NACA 0012 cascade and -0.408 at $\sigma = 60$ deg. (superresonant) for the "classical" flat plate configuration. Hence, at least for this example, the effect of blade geometry is to cause a substantial reduction in torsional stability margin. In addition, the predictions at the lower frequency ($\omega = 0.5$) indicate that the NACA 0012 cascade will experience subresonant torsional instabilities (according to linear aerodynamic theory) at low vibration frequencies.

CONCLUDING REMARKS

The aerodynamic analysis described here has been developed to determine the flow past a finite-deflection, oscillating cascade operating in subsonic free-stream conditions. This analysis is intended to serve as a basis for investigating flutter or free vibration phenomena in jet engine fan, compressor and turbine blade rows. The unsteady aerodynamic model assumes small-amplitude fluctuations about a nonuniform steady flow and fully accounts for the effects of blade geometry and steady flow turning on the response to an oscillating cascade in fully-attached subsonic flow. The steady flow is governed by the full-potential, boundary value problem and the unsteady flow is governed by a linear boundary value problem with variable coefficients defined by the steady flow. With the present formulation a numerical resolution of time-independent, linear, unsteady equations is required only over a single extended blade-passage region of finite extent. Further, an incompressible model problem study (cf. the APPENDIX) indicates that the first-order or unsteady flow is analytic, but rapidly varying, near a blunt leading or trailing edge, and is thus susceptible to numerical resolution provided that a sufficiently detailed computation grid is employed in such regions.

The unsteady numerical model is general and comprehensive enough to approximate accurately the unsteady equations despite the difficulties posed by cascade periodicity, nonrectangular geometry, and limited regions of rapid flow variation. Differential quantities are approximated in the physical plane using finite differences determined by an implicit least-squares interpolation and applicable on arbitrary grids. The approximation is flexible enough so that neighbor sets can be adjusted to accommodate singular behavior near blade edges, and both differential equation and boundary condition can be simultaneously approximated at boundary points. In general, the unsteady equations are first solved on a nonorthogonal, body-fitted, and periodic cascade mesh (Fig. 3), and then on dense local meshes in regions of large velocity gradient (e.g., near a blunt leading edge, Fig. 4). On either cascade or local mesh, the unsteady boundary value problem is approximated by a block-tridiagonal system of linear algebraic equations which is solved by direct matrix inversion .

In previous studies unsteady solutions were determined on a cascade mesh for cascades of sharp-edged blades with mean camber lines aligned with the steady flow (Refs. 7, 11). Predictions for flat plate cascades have been shown to be in good agreement with Smith's (Ref. 2) analytical results for both subresonant and superresonant blade motions. Further, predictions for double-circular-arc blades revealed that blade thickness produces a strong coupling between steady and unsteady flows, particularly at high Mach number or low vibration frequency.

Under the present effort the solution procedure has been extended and applied to cascades of blunt leading-edged airfoils at incidence relative to the inlet flow. Results have been presented here for cascades of NACA 0012 airfoils to

demonstrate solution capability and to further illustrate the influence of blade geometry (including leading edge curvature), Mach number, and incidence on unsteady response. Cascade and local mesh solutions indicate that leading edge curvature effects must be taken into account to accurately predict the unsteady force and moment components in-phase with blade displacement. Detailed local solutions for the NACA 0012 profiles provide unsteady pressure difference distributions which are zero at the leading edge and reach maximum or minimum values at distances from the leading edge on the order of the leading edge radius. Results for staggered and unstaggered cascades of flat plate and NACA 0012 airfoils reveal that unsteady aerodynamic response is strongly dependent on blade thickness distribution and inlet Mach number. In particular, the stability margin for torsional motions of staggered (Θ = 45 deg.) cascades is substantially less for the NACA 0012 than for the flat plate cases. The stability of out-of-phase bending or torsional vibrations is enhanced with increasing Mach number for both NACA 0012 and flat plate cascades, but particularly for the former. Finally, for subsonic attached flow past NACA 0012 cascades, mean incidence appears to have only a slight effect on unsteady force or moment. However, inlet flow angle variations do cause substantial changes in unsteady pressure distribution near blade leading edges.

Future Studies

Further developments in the unsteady aerodynamic analysis will be required before a comprehensive flutter prediction scheme can be realized. For the subsonic Mach number range in which blade vibrations are of practical concern, it will be necessary to extend the present analysis to include transonic flows with weak shocks. For transonic applications, shock motion conditions (Ref. 24) must be incorporated into the aerodynamic model and appropriate differencing procedures for supersonic regions must be determined for the unsteady numerical model. In addition, for vibrating thin fan or compressor blades at incidence - the positive incidence flutter problem (Ref. 25) - it appears that the aerodynamic model will have to be modified to incorporate the effects of viscous-induced, leading-edge, separation bubbles. Progress in this direction is heavily dependent on advances in the calculation of steady cascade flows. Finally, the aerodynamic analysis developed to predict cascade flutter or free vibration phenomena should be combined with solutions of the vorticity and entropy transport equations (cf. Refs. 26, 27) to provide an analysis for the prediction of forced excitation phenomena in turbomachinery blade rows.

APPENDIX

INCOMPRESSIBLE MODEL PROBLEM

Certain restrictions are inherent to a perturbation approximation. If these are not satisfied throughout the solution domain, the perturbation expansion is said to be singular, i.e., the asymptotic series does not provide a uniformly valid approximation to the true solution (Ref. 17). In classical linear theory this situation is manifested by analytical singularities (i.e., $|\nabla\phi| \sim \mathcal{O}(r_E^{n/2})$ where r_E is the distance from the edge) in the first order solution at airfoil leading (n=-1/2) and trailing (n = 1/2) edges (Ref. 19). To clarify both the convergence properties of the asymptotic series associated with the present aerodynamic model (Eq. (5)) and the behavior of the first-order solution, especially in the vicinity of blunt leading edges, a quasi-steady ($\omega \to 0$), incompressible ($M_\infty \to 0$) flow has been studied. The results of this study provide important considerations for a successful numerical resolution of the first-order unsteady flow field.

Consider incompressible flow past an elliptic airfoil, $\mathcal{S}$, which has undergone a rigid displacement from an original or mean position, S (Fig. 20). The latter is situated at angle of attack A relative to the uniform stream, $\vec{V}_\infty$. Body-fixed ξ, η - and x,y-coordinate axes coincide with the major and minor axes of the ellipses $\mathcal{S}$ and S, respectively. Hence, $\zeta = (z-h)e^{-i\alpha}$ where $\zeta = \xi + i\eta$, $z = x + iy$, $h = h_x + ih_y$ defines the amplitude and direction of the translational displacement, and α defines the amplitude and direction of the rotational displacement about $\zeta = 0$. The complex potential, $\hat{W}$, for the flow about the displaced ellipse, $\mathcal{S}$, is given by (Refs. 28, 29)

$$(1-b)\hat{W}(\zeta) = H(\zeta, \hat{A}) = F(\zeta)\cos\hat{A} - i\,G(\zeta)\sin\hat{A} + i(1-b)\hat{\Gamma}\ln\left[\frac{\zeta + \sqrt{\zeta^2 - 4a^2}}{2}\right] \tag{A1}$$

where

$$F(\zeta) = \zeta - b\sqrt{\zeta^2 - 4a^2}\,, \quad G(\zeta) = b\zeta - \sqrt{\zeta^2 - 4a^2} \tag{A2}$$

$$\hat{\Gamma} = -(1+b)\sin\hat{A}/2$$

$\hat{A} = A + \alpha$, b is the thickness of the airfoil, $a = (1 - b^2)^{1/2}/4$, and $\hat{\Gamma}$ is the circulation. The circulation has been specified by requiring that the rear stagnation point occurs at the trailing edge ($\zeta = 1/2$). For b = 0, Eq. (A1) defines the complex potential for the flow past a flat plate at angle of attack, $\hat{A}$, relative to the

uniform stream $\vec{V}_\infty$. In this case the prescribed circulation, Eq. (A2), guarantees that the flow does not stagnate near the trailing edge of the airfoil.

Perturbation Solution

The complex potential can be formally expressed as a power series in the parameter ϵ; i.e.,

$$\hat{W}(\zeta) = \sum_{j=0}^{\infty} \epsilon^j w_j(z) = W(z) + w(z) + \mathcal{O}(\epsilon^2) \tag{A3}$$

where ϵ depends on the displacement of the airfoil $\mathcal{S}$ from its original or mean position. The first two terms of this series are determined explicitly by expanding the second term on the right-hand-side of the expression

$$(\zeta^2 - 4a^2) = (z^2 - 4a^2)\left[1 + \frac{(\zeta^2 - z)^2}{z^2 - 4a^2}\right] \tag{A4}$$

in a binomial series; i.e.,

$$\left[1 + \frac{(\zeta^2 - z^2)}{z^2 - 4a^2}\right]^{1/2} = 1 + \frac{\zeta^2 - z^2}{2(z^2 - 4a^2)} + \cdots \tag{A5}$$

substituting this result along with the series expansions for $\cos\alpha$ and $\sin\alpha$ into Eq. (A1), and neglecting second and higher order terms in h_x, h_y, and α. After some algebra it follows that

$$(1-b)\,W(z) = H(z, A) \tag{A6}$$

and

$$\begin{aligned}(1-b)\,w(z) &= \alpha \frac{\partial H}{\partial A} - s\frac{\partial H}{\partial z} \\ &= -\alpha F(z)\sin A - i\alpha\left[G(z) + \frac{(1-b^2)}{2}\ln\left(\frac{z+\sqrt{z^2-4a^2}}{2}\right)\right]\cos A \\ &\quad + s\left[G(z)\cos A - i(F(z) - (1-b^2)/2)\sin A\right]\Big/\sqrt{z^2-4a^2}\end{aligned} \tag{A7}$$

where $s = h + i\alpha z$. Thus, $W(z)$ is the complex potential of the flow past the ellipse S and $w(z)$ is the linear (in α, h_x and h_y) approximation to the change in this solution due to a rigid-body displacement.

The power series, Eq. (A3) evaluated at the point z, converges to the exact solution, $\hat{W}$, evaluated at $\zeta = (z-h)e^{-i\alpha}$ for flow past the displaced ellipse, $\mathcal{S}$, if

$$\left|\zeta^2 - z^2\right| = \left|(z-h)^2 e^{-2i\alpha} - z^2\right| < \left|z^2 - 4a^2\right| = \left|z+2a\right|\left|z-2a\right| \tag{A8}$$

at each point z on or exterior to S. The foregoing inequality can be expressed in the form

$$|s| < \frac{|z+2a||z-2a|}{2|z|} - O(|s|^2) \tag{A9}$$

Thus, the power series, Eq. (A3), converges if the distance from z to ζ is small compared to the ratio of the product of the distances from z to the foci (at $z = \pm 2a$) of the ellipse S to twice the distance from z to the origin ($z = 0$). In particular, at the edges of the airfoil ($z = \pm 1/2$), the foregoing inequality reduces to

$$\left|h \pm ia/2\right| < b^2/4 - O(|s|^2) \tag{A10}$$

where $b^2/4$ is the edge radius. Thus, for sufficiently small displacements, the power series, Eq. (A3), will converge throughout the flow field, and the first two terms of this series will provide a valid first-order approximation to the flow past the displaced ellipse. If condition (A10) is not satisfied (e.g., for a flat plate airfoil), the perturbation approximation is singular near the edges of the airfoil.

The zeroth-and first-order complex velocities are given by

$$(1-b)\frac{dW}{dz} = \frac{\partial H}{\partial z} = -(z^2-4a^2)^{-1/2}\left[G(z)\cos A - i\left[F(z)-(1-b^2)/2\right]\sin A\right] \tag{A11}$$

and

$$\begin{aligned}(1-b)\frac{dw}{dz} = a\frac{\partial^2 H}{\partial A\,\partial z} - s\frac{\partial^2 H}{\partial z^2} &= ia e^{-iA}(z-4a^2)^{-1/2}\left[G(z)+F(z)-(1-b^2)/2\right] \\ &\quad -s(z^2-4a^2)^{-1}\left[F(z)\cos A - i\,G(z)\sin A\right] \\ &\quad -sz(z^2-4a^2)^{-3/2}\left[G(z)\cos A - i\left[F(z)-(1-b^2)/2\right]\sin A\right]\end{aligned} \tag{A12}$$

For flow past a displaced ellipse the zeroth-and first-order complex velocities are analytic. They behave like multiples of $z_C^{-1/2}$ and $z_C^{-3/2}$, respectively, near the blunt leading and trailing edges of the airfoil, where z_C is a complex coordinate measured from the center of the edge circle. For a flat plate airfoil (b=0, a = 1/4) the zeroth order complex velocity has a square-root singularity ($dW/dz \sim \mathcal{O}(z+1/2)^{-1/2}$) at the leading edge and behaves like a multiple of $(z - 1/2)^{1/2}$ at the trailing edge. In addition, the first-order velocity is singular like a multiple of $(z + 1/2)^{-3/2}$ at the leading edge and like a multiple of $(z - 1/2)^{-1/2}$ at the trailing edge. For a flat plate at zero mean angle of attack (the classical linear problem) $dW/dz = 1$, and the order of the singularities in the first-order complex velocity is reduced by one (i.e., $dw/dz \sim (z + 1/2)^{-1/2}$ at the leading edge and $dw/dz \sim (z - 1/2)^{1/2}$ at the trailing edge).

Governing Boundary Value Problems

Since the zeroth order term, W(z) of the series expansion, Eq. (3), is the complex potential for the flow past the ellipse S (Fig. 1), $\Phi = \mathrm{Re}\{W(z)\}$ is a solution of Laplace's equation which satisfies the following boundary conditions

$$\nabla \Phi \cdot \vec{n} = 0, \qquad \text{on } S \tag{A13}$$

and

$$\lim_{|z| \to \infty} \nabla \Phi = \cos A \, \vec{e_x} + \sin A \, \vec{e_y} \tag{A14}$$

where $\vec{n}$ is a unit outward normal vector and $\vec{e}_x$ and $\vec{e}_y$ are unit vectors in the coordinate directions. The first-order velocity potential, $\phi = \mathrm{Re}\{w(z)\}$, is also a solution of Laplace's equation, and it can be verified that $\phi(x,y)$ meets the following conditions

$$\nabla \phi \cdot \vec{n} = \left[\vec{\alpha} \times \nabla \Phi - (\vec{r} \cdot \nabla) \nabla \Phi\right] \cdot \vec{n}, \qquad \text{on } S \tag{A15}$$

and

$$\lim_{|z| \to \infty} \nabla \phi = 0 \tag{A16}$$

where $\vec{r} = (h_x + \alpha y)\,\vec{e}_x + (h_y - \alpha x)\,\vec{e}_y$. Thus exact solutions to the steady and the linear unsteady boundary value problems described in this report (c.f. Eqs. (1), (3), (8), (9) and (11)) have been determined for the flow past an isolated elliptic airfoil in the limiting case $M_{-\infty} \to 0$ and $\omega \to 0$. Note that the unsteady boundary conditions of continuous normal velocity and pressure across the wake (Eq. (12)) are automatically satisfied since $\nabla\phi$ is continuous throughout the flow. Further, the unsteady far-field conditions (Eqs. (14) and (16)) are replaced by the condition that the first-order velocity vanishes far from the airfoil. The zeroth-and first-order pressures acting on the displaced airfoil, $\mathcal{S}$, follow from Eqs. (2), (18) and (19) for $M_{-\infty} \to 0$ and $\omega \to 0$ and are given by

$$P_S = P_{-\infty} + 1 - (\nabla\Phi)_S^2 \tag{A17}$$

and

$$P_{\mathcal{S}} = \left[-2\nabla\Phi\cdot\nabla\phi + \vec{r}\cdot\nabla P\right]_S = \left[-2\nabla\Phi\cdot\nabla\phi - \vec{r}\cdot\nabla(\nabla\Phi)^2\right]_S \tag{A18}$$

The zeroth-and first-order solutions, Eqs. (A6) and (A7), have been programmed and sample results for the first-order potential and normal velocity on the mean surface, S, and the first-order pressure difference are shown for rotational displacements with $\alpha = 2$ in Figs. 21 through 25. Surface velocity potential distributions for flat plate ($b = 0$) and elliptic airfoils ($b = 0.1$ and $b = 0.2$) at zero mean angle of attack, A, are depicted in Fig. 21. In each case the potential varies gradually over most of the airfoil, but abrupt changes in potential occur near the leading and trailing edges of the elliptic airfoils. The magnitude of these rapid changes increase with decreasing thickness (for $b \neq 0$) and with increasing magnitude of angle of attack. In contrast, abrupt changes in surface potential do not occur for a flat plate airfoil.

Surface normal velocity distributions, as determined from the first-order flow tangency condition, are shown in Figs. 22 and 23 for flat plate and elliptic airfoils at 0 deg. and -10 deg. mean angles of attack. Details in the vicinity of the leading edge are shown in the latter figure. Results for the flat plate at A = 0 (i.e., $\nabla\phi \cdot \vec{n}|_S = \pm 2$) correspond to the classical-linear-theory boundary condition. The effects of thickness or non-zero mean angle of attack is to cause large and rapid variations in first-order normal velocity in the vicinity of airfoil edges. These variations increase with decreasing thickness for $b \neq 0$ or increasing magnitude of angle of attack. For the flat plate at A = -10 deg. the surface normal velocity distribution is singular at the leading edge and varies monotonically with

distance from the leading edge along the upper and lower surfaces of the airfoil. However, for the elliptic airfoil the variations in first-order normal velocity along the upper and lower surfaces change sign near the edges of the airfoil (Fig. 22). This behavior has an important impact on the numerical resolution of the first-order flow and will be discussed in more detail below.

First-order pressure-difference distributions, $\Delta p(x)$, due to rotational displacements with $\alpha = 2$, for symmetric mean flows ($A = 0$) past flat plate airfoil and elliptic airfoils with $b = 0.1$ and $b = 0.2$, and for flow past an ellipse with $b = 0.1$ at -10 deg. mean angle of attack are shown in Fig. 24. Leading edge details are provided in Fig. 25. The results depicted in Fig. 24 suggest that the first-order loading (i.e., Δp or c_L) is more dependent on airfoil thickness than on mean angle of attack. Significant variations in the first-order pressure difference occur near the edges of the airfoil, particularly near the leading edge. For the blunt-edged airfoils the pressure difference distributions reach minimum values at a distance of $b^2/4$ from the leading edge; i.e., at a distance equal to the leading edge radius (Fig. 25).

Inner and Outer Expansions

The results depicted in Figs. (21) through (25) indicate that flow parameters vary sharply in the vicinity of airfoil edges and gradually over the remainder of the chord. This behavior suggests that the flow past an elliptic airfoil depends on two length scales — the edge radius, $b^2/4$, and the square root of the product of the distances from a given point, z, to the leading and trailing edges; i.e., $(z^2 - 1/4)^{1/2}$. Approximations to the zeroth-and first-order complex velocities, based on this concept, can be determined. An "inner" solution valid in a neighborhood of the leading edge, $|z_C| \sim \mathcal{O}(b^2)$ where $z_C = z + 2a$, is obtained by substituting the expansion

$$(z^2-4a^2)^n \sim (-\sqrt{1-b^2})^n \, z_C^{\,n} \left[1 - nz_C/\sqrt{1-b^2} + \mathcal{O}(|z_C|^2)\right] \tag{A19}$$

into Eqs. (A2), (A11) and (A12). It follows after some algebra that for $A \sim \mathcal{O}(b) \ll 1$

$$(1-b)\left.\frac{dw}{dz}\right|_I \sim 1 - (A + ib/2)\, z_C^{-1/2} + \mathcal{O}(b^2) \tag{A20}$$

and

$$(1-b)\left.\frac{dw}{dz}\right|_I \sim -s(A + ib/2)\, z_C^{-3/2}/2 - \alpha\, z_C^{-1/2} + \mathcal{O}(|s|) \tag{A21}$$

Thus, as noted previously, the zeroth-and first-order complex velocities exhibit a $z_C^{-1/2}$ and a $z_C^{-3/2}$ behavior, respectively, in the vicinity of a blunt leading edge.

Similarly, an "outer" approximation, valid in the region $|z^2 - 1/4| \sim \mathcal{O}(1)$, is determined by substituting the expansion

$$(z^2-4a^2)^n \sim (z^2-1/4)^n \left[1+nb^2(z^2-1/4)^{-1}/4\right] + \mathcal{O}(b^4) \tag{A22}$$

into the exact expressions for the zeroth-and first-order complex velocities. It follows for $A \sim \mathcal{O}(b) << 1$ that

$$(1-b)\frac{dw}{dz}\bigg|_0 \sim 1+(z^2-1/4)^{-1/2}\left[iA(z-1/2)-bz\right] + \mathcal{O}(b^2) \tag{A23}$$

and

$$(1-b)\frac{dw}{dz}\bigg|_0 \sim -a\left[A+i(1+b)\right]\left[1-(z-1/2)^{1/2}(z+1/2)^{-1/2}\right] \tag{A24}$$

$$+ s\left\{(b+iA)(z^2-1/4)^{-1/2} + z\left[i(z-1/2)A-bz\right](z^2-1/4)^{-3/2}\right\} + \mathcal{O}(|s|b^2)$$

Equation (A23) is the classical first-order approximation for the flow past an ellipse of thickness b situated at angle of attack A relative to a uniform stream. It can be shown that the outer first-order solution satisfies the first-order flow tangency condition, Eq. (A15), when the steady velocity is obtained from the outer approximation to the zeroth order solution, Eq. (A23). It follows from Eqs. (A18), (A23) and (A24) that the outer approximation to the pressure difference across the airfoil is

$$\Delta p(x)\Big|_0 = -4a\left[(1/2-x)+b(1-3x)\right](1/4-x^2)^{-1/2} + \mathcal{O}(|s|b^2) \tag{A25}$$

Therefore, to lowest order $\Delta p(x)\Big|_0$ for the displaced airfoil depends on airfoil thickness, b, but not on mean angle of attack, A .

Near the leading edge of the airfoil ($z_{LE} \sim \mathcal{O}(b^2)$) the outer solution assumes the form

$$(1-b)\left.\frac{dw}{dz}\right|_0 \sim 1 - (A+ib/2)\, z_{LE}^{-1/2} + \cdots \qquad \text{(A26)}$$

and

$$(1-b)\left.\frac{dw}{dz}\right|_0 \sim -s(A+ib/2)z_{LE}^{-3/2}/2 - \alpha z_{LE}^{-1/2} + \cdots \qquad \text{(A27)}$$

where $z_{LE} = z + 1/2 = z_C + b^2/4$. Thus, to lowest order the inner and outer solutions have the same functional form near the leading edge of the airfoil. The inner solutions depend on the variable z_C which is measured from the center of the leading edge circle, while the outer solutions depend on z_{LE} which is measured from the leading edge of the airfoil.

Closure

The foregoing model-problem study reveals several important features of perturbation solutions to airfoil type flows. In particular, the solution for the flow past a displaced airfoil can be represented as an asymptotic series in which the zeroth order solution describes the flow past the airfoil at its original location and the remaining terms account for the effects of the displacement. This series will converge to the exact solution for the flow past the displaced airfoil if the displacement is small compared to the edge radii of the airfoil. If this criterion is not met, but the displacement is still sufficiently small, the asymptotic series will converge everywhere except near the edges of the airfoil. In this case the perturbation approximation is singular. In either event the first-order term of the asymptotic series is a solution of a linear boundary value problem in which the airfoil surface boundary condition (i.e., the flow tangency condition) is satisfied on the original airfoil surface. The zeroth-and first-order solutions are analytic for blunt-edged airfoils, but these potentials, or their derivatives to some order, are singular at sharp leading and trailing edges. Finally, near blade edges, the zeroth-and first-order solutions are essentially functions of a position vector emanating from the center of the edge circle.

Numerical Implications

One purpose in conducting the model-problem study is to provide guidance for the numerical resolution of unsteady cascade flows. First-order results depicted in Figs. 21 through 25 indicate that with the exception of small neighborhoods surrounding the blade edges, the first-order unsteady flow could be captured on a relatively coarse rectilinear type mesh which covers the extended blade passage region; e.g., the mesh shown in Fig. 3. Although this mesh is generally well suited for approximating conditions on the boundaries of the extended blade passage region, and for capturing the unsteady flow throughout most of the solution domain, it is not suitable for resolving the flow in the vicinity of blunt blade edges. As a result solutions to the unsteady-cascade boundary value problem were initially reported for sharp-edged profiles (Refs. 7 and 11). For a blunt-edged airfoil, a solution on the cascade mesh must be supplemented by local solutions on very fine meshes (e.g., Fig. 4) in regions where velocity gradients are large. The coarse mesh solution is then used to provide conditions on the outer boundary of the local mesh. A prerequisite for this approach is the ability to determine a reasonably accurate unsteady solution on the coarse mesh.

The present authors' early attempts to resolve the unsteady boundary value problem for blunt leading-edged, compressor-type, airfoils on the cascade mesh (Fig. 3) resulted in spurious unsteady pressure predictions over the entire airfoil including violent pressure oscillations near the leading edge. Results of the model problem study reveal the source of difficulty to be the partial inclusion of local phenomena in the coarse mesh calculation. Since this mesh should only be used to calculate an "outer" approximation to the unsteady flow field, local steady flow behavior should be excluded from the governing differential equation, Eqs. (9, 10), and surface boundary condition, Eq. (11), for the coarse mesh calculation. This is accomplished by not placing mesh lines too close to a blunt leading edge, and by replacing the local steady flow solution by an approximate outer solution in the vicinity of blade leading edges. That is, the functional dependence of steady potential derivatives on a position vector emanating from the center of the leading edge circle, $\vec{r}_c$, is replaced by a functional dependence on a position vector emanating from the leading edge, $\vec{r}_{LE}$, to produce singular, but monotonic (near $\vec{r}_{LE} = 0$) behavior in steady potential derivatives along radial lines emanating from the leading edge. Such behavior poses no difficulty to the calculation of coarse mesh solutions. The unsteady numerical solution on the coarse mesh is then akin to an outer unsteady solution, and as such, it provides reasonably accurate boundary condition information for determining an inner solution on a dense local mesh surrounding a blunt leading edge. Similar considerations should be applied to calculate the unsteady flow past a cascade of airfoils with blunt trailing edges.

REFERENCES

1. Kaji, S., and T. Okazaki: Propagation of Sound Waves Through a Blade Row, II. Analysis Based on the Acceleration Potential Method. Journal of Sound and Vibration, Vol. II, No. 3, March 1970, pp. 335-375.

2. Smith, S. N.: Discrete Frequency Sound Generation in Axial Flow Turbomachines. R&M 3709, British Aeronautical Research Council, London, England, 1971.

3. Verdon, J. M.: Further Developments in the Aerodynamic Analysis of Unsteady Supersonic Cascades: Parts 1 and 2. Transactions of the ASME: Journal of Engineering for Power, Series A, Vol. 99, No. 4, October 1977, pp. 509-525.

4. Adamczyk, J. J. and M. E. Goldstein: Unsteady Flow in a Supersonic Cascade with Subsonic Leading-Edge Locus. AIAA Journal, Vol. 16, No. 12, December 1978, pp. 1248-1254.

5. Namba, M.: Subsonic Cascade Flutter with Finite Mean Lift. AIAA Journal, Vol. 13, No. 5, May 1975, pp. 586-593.

6. Verdon, J. M., J. J. Adamczyk, and J. R. Caspar: Subsonic Flow Past an Oscillating Cascade with Steady Blade Loading - Basic Formulation. Unsteady Aerodynamics, R. B. Kinney (ed.), Proceedings of a Symposium held at the University of Arizona, Tucson, Arizona, March 1975, Vol. II, pp. 827-851.

7. Verdon, J. M. and J. R. Caspar: Subsonic Flow Past an Oscillating Cascade with Finite Mean Flow Deflection. AIAA Journal, Vol. 18, No. 5, May 1980, pp. 540-548.

8. Caspar, J. R., D. E. Hobbs, and R. L. Davis: Calculation of Two-Dimensional Potential Cascade Flow Using Finite Area Methods. AIAA Journal, Vol. 18, January 1980, pp. 103-109.

9. Ives, D. C. and J. F. Liutermoza: Analysis of Transonic Cascade Flow Using Conformal Mapping and Relaxation Techniques. AIAA Journal, Vol. 15, May 1977, pp. 647-652.

10. Ives, D. C. and J. F. Liutermoza: Second Order Accurate Calculation of Transonic Flow over Turbomachinery Cascades. AIAA Journal, Vol. 17, August 1979, pp. 870-876.

11. Caspar, J. R. and J. M. Verdon: Numerical Treatment of Unsteady Subsonic Flow Past an Oscillating Cascade. Paper No. 80-1428, AIAA 13th Fluid & Plasma Dynamics Conference, Snowmass, Colorado, July 14-16, 1980.

REFERENCES (Continued)

12. Guiraud-Vallee, D., et al.: Numerical Studies of Unsteady Inviscid Flows at ONERA. Paper presented at the Conference on Numerical Methods and Fluid Dynamic Applications, University of Reading, Great Britain, January 4-6, 1978.

13. Atassi, H., and T. J. Akai: Effect of Blade Loading and Thickness on the Aerodynamics of Oscillating Cascades. Paper No. 78-227, AIAA 16th Aerospace Sciences Meeting, Huntsville, Alabama, January 16-18, 1978.

14. Atassi, H. and T. J. Akai: Aerodynamic Force and Moment on Oscillating Airfoils in Cascade. Paper No. GT-181, ASME Gas Turbine Conference, London, England, April 9-13, 1978.

15. Whitehead, D. S., and R. J. Grant: Force and Moment Coefficients for High Deflection Cascades. University of Cambridge, Department of Engineering Report CUED/A-Turbo/TR 98, Cambridge, England, May, 1980.

16. Ni, R. H., and F. Sisto: Numerical Computation of Nonstationary Aerodynamics of Flat Plate Cascades in Compressible Flow. Transactions of the ASME: Journal of Engineering for Power, Series A, Vol. 98, No. 2, April 1976, pp. 165-170.

17. Van Dyke, M.: Perturbation Methods in Fluid Mechanics. Academic Press, New York, 1964, pp. 45-73.

18. Carta, F. O.: Coupled Blade - Disk - Shroud Flutter Instabilities in Turbojet Engine Rotors. Transactions of the ASME, Journal of Engineering for Power, Series A, Vol. 89, No. 3, July 1967, pp. 419-427.

19. Ashley, H., and M. Landahl: Aerodynamics of Wings and Bodies. Addison-Wesley Publishing Co., Inc., Reading, Massachusetts, 1965, p. 93 and pp. 245-249.

20. Varga, R. S.: Matrix Iterative Analysis. Prentice-Hall, Inc., Englewood Cliffs, New Jersey, 1965, p. 196.

21. Van Dine, C. P.: An Algorithm for the Optimization of Trajectories with Associated Parameters. AIAA Journal, Vol. 7, March 1969, pp. 400-405.

22. Abbott, I. H. and A. E. Von Doenhoff: Theory of Wing Sections. Dover Publications, New York, 1959.

REFERENCES (Concluded)

23. Fung, Y. C.: An Introduction to the Theory of Aeroelasticity. John Wiley and Sons, Inc., New York, 1955, pp. 166-168.

24. Fung, K. Y., N. J. Yu, and R. Seebass: Small Unsteady Perturbations in Transonic Flows. AIAA Journal, Vol. 16, No. 8, pp. 815-822, August 1978.

25. Mikolajczak, A. A., R. A. Arnoldi, L. E. Snyder, and H. Stargardter: Advances in Fan and Compressor Blade Flutter Analysis and Predictions. Journal of Aircraft, Vol. 12, No. 4, April 1975, pp. 325-332.

26. Adamczyk, J. J.: The Passage of a Distorted Velocity Field Through a Cascade of Airfoils. AGARD-CPP-177, pp. 31-1 through 31-14, 1975.

27. Goldstein, M. E.: Unsteady Vortical and Entropic Distortions of Potential Flows Round Arbitrary Obstacles. Journal of Fluid Mechanics, Vol. 89, Part 3, pp. 433-468, 1978.

28. Rutherford, D. E.: Fluid Dynamics. Interscience Publishers Inc., New York, 1959, pp. 58-64.

29. Milne-Thomson, L. M.: Theoretical Hydrodynamics. The Macmillan Company, New York, pp. 159-167, 1960.

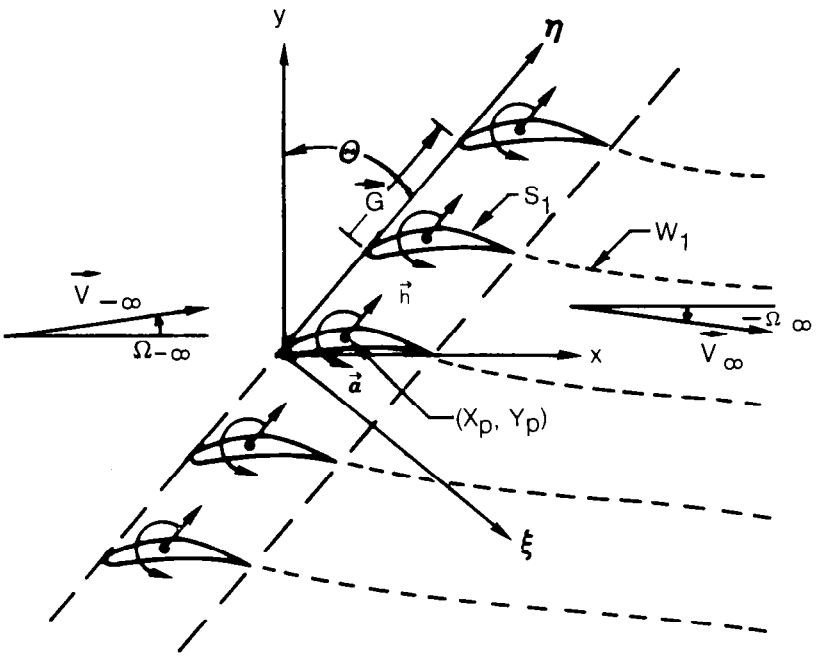

Fig. 1 Two-Dimensional Oscillating Cascade with Finite Mean-Flow Deflection

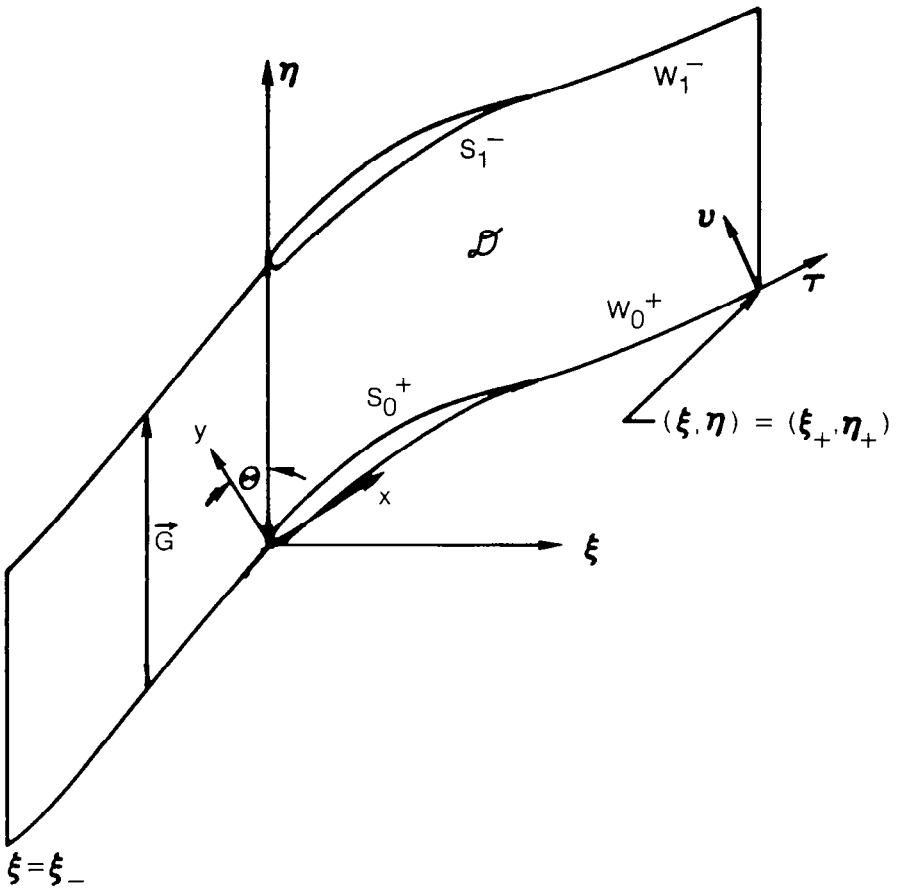

Fig. 2 Extended Blade-Passage Region

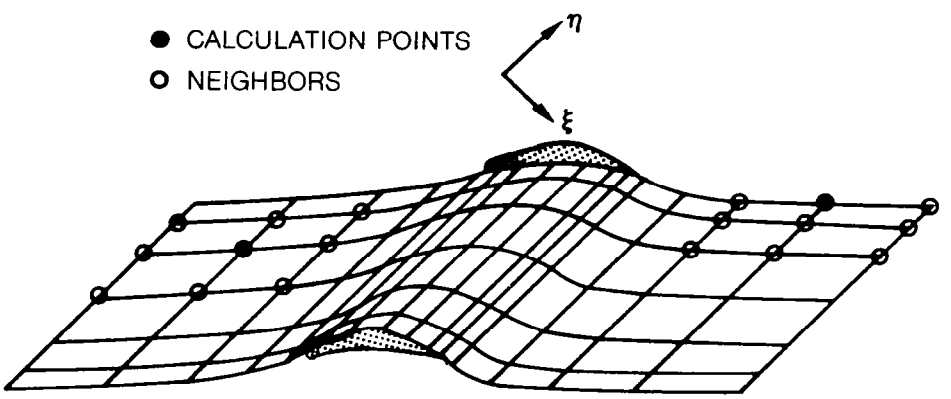

Fig. 3 Cascade Mesh

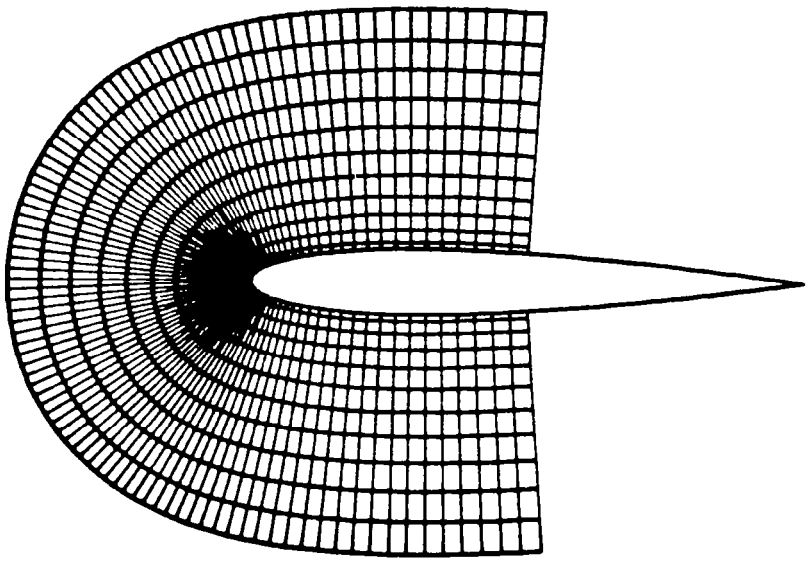

Fig. 4 Local Mesh

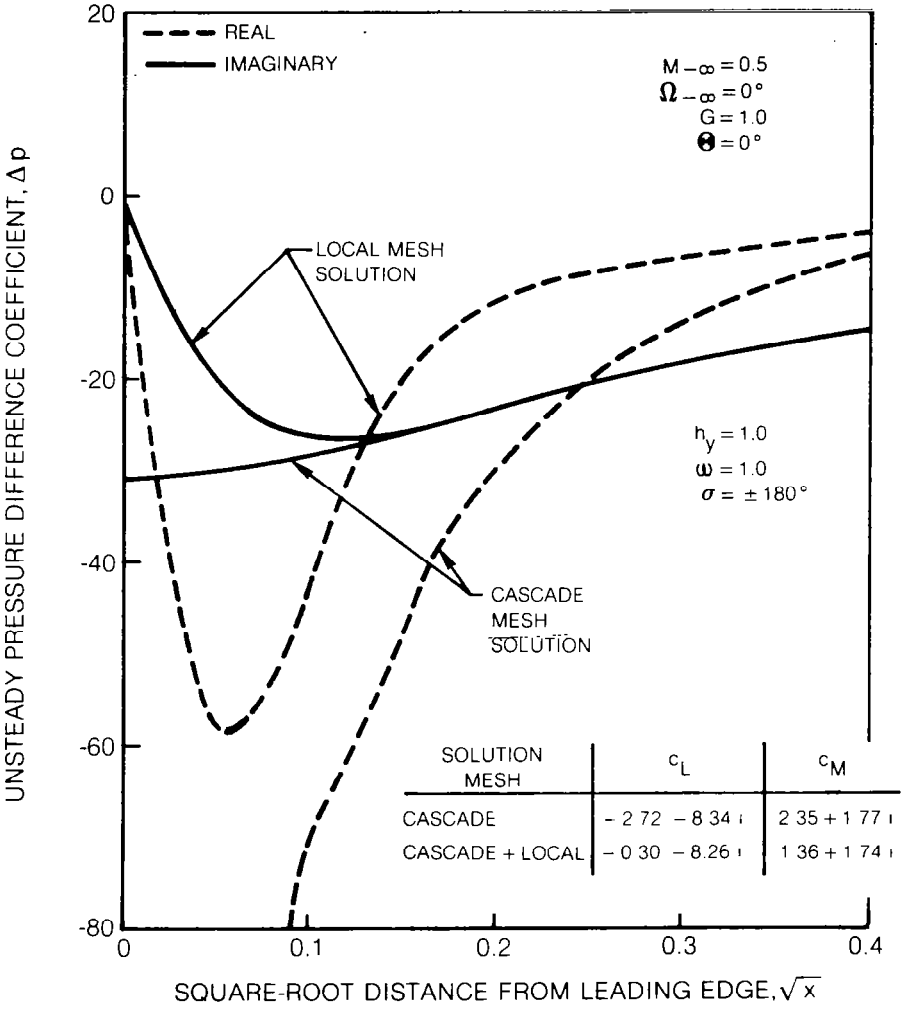

Fig. 5 Unsteady Pressure Difference near the Leading Edge of a NACA 0012 Blade Due to Bending

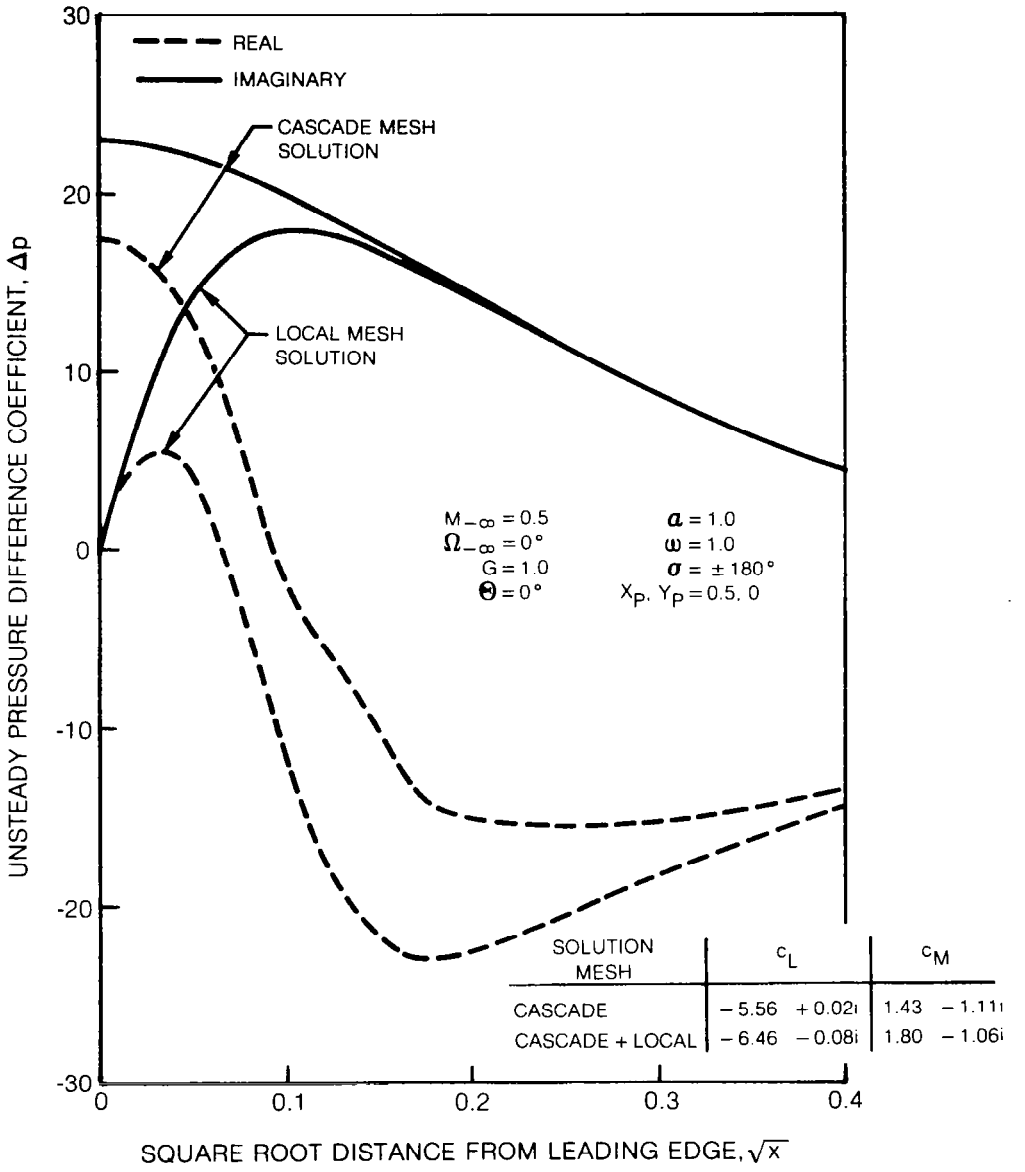

Fig. 6 Unsteady Pressure Difference near the Leading Edge of a NACA 0012 Blade Due to Torsion

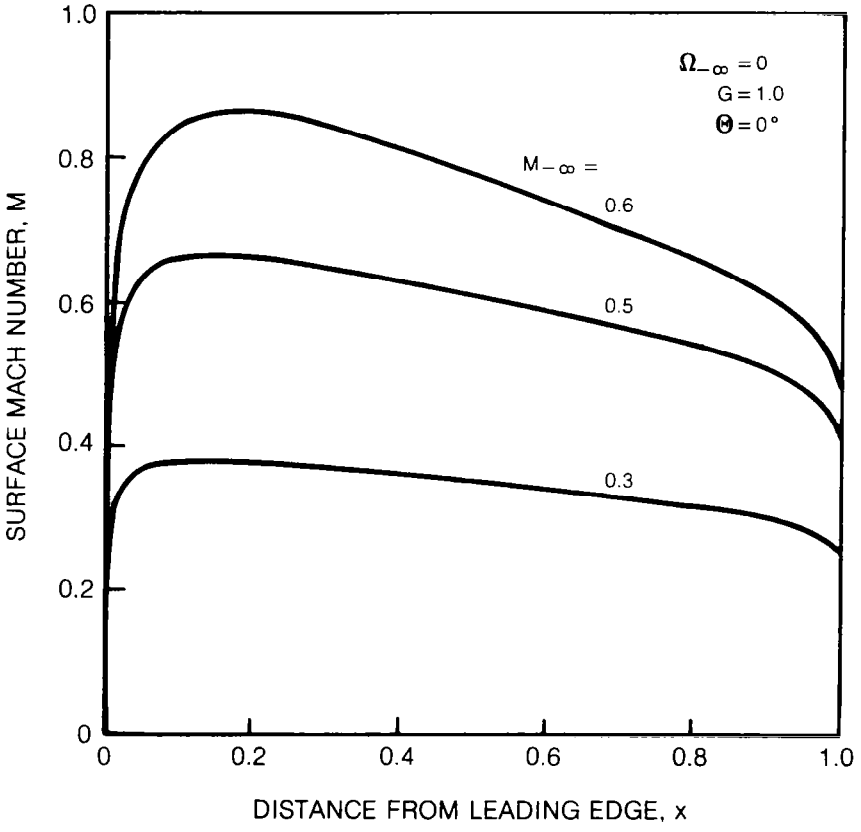

Fig. 7 Surface Mach Number Distribution for an Unstaggered Cascade of NACA 0012 Airfoils

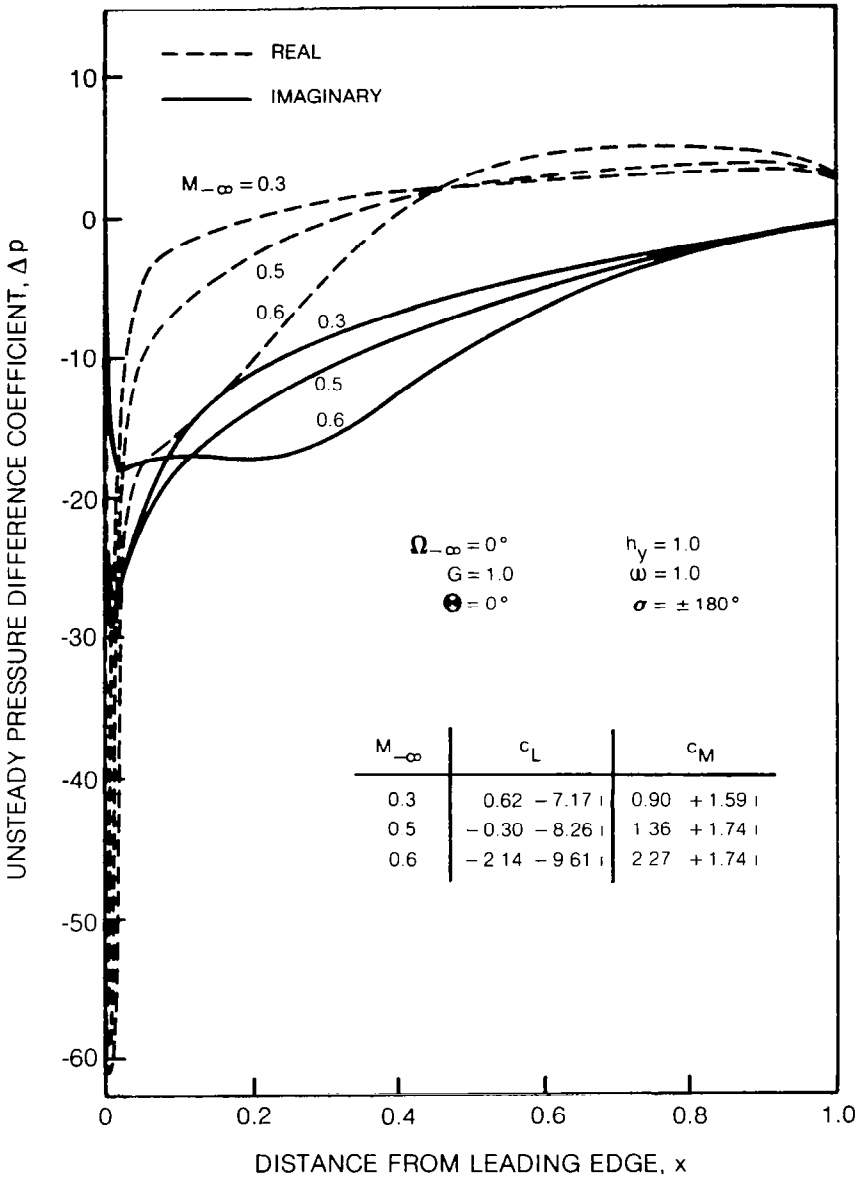

$M_{-\infty}$	c_L	c_M
0.3	0.62 − 7.17 i	0.90 + 1.59 i
0.5	−0.30 − 8.26 i	1.36 + 1.74 i
0.6	−2.14 − 9.61 i	2.27 + 1.74 i

Fig. 8 Effect of Inlet Mach Number on Unsteady Response Due to Bending for an Unstaggered Cascade of NACA 0012 Airfoils

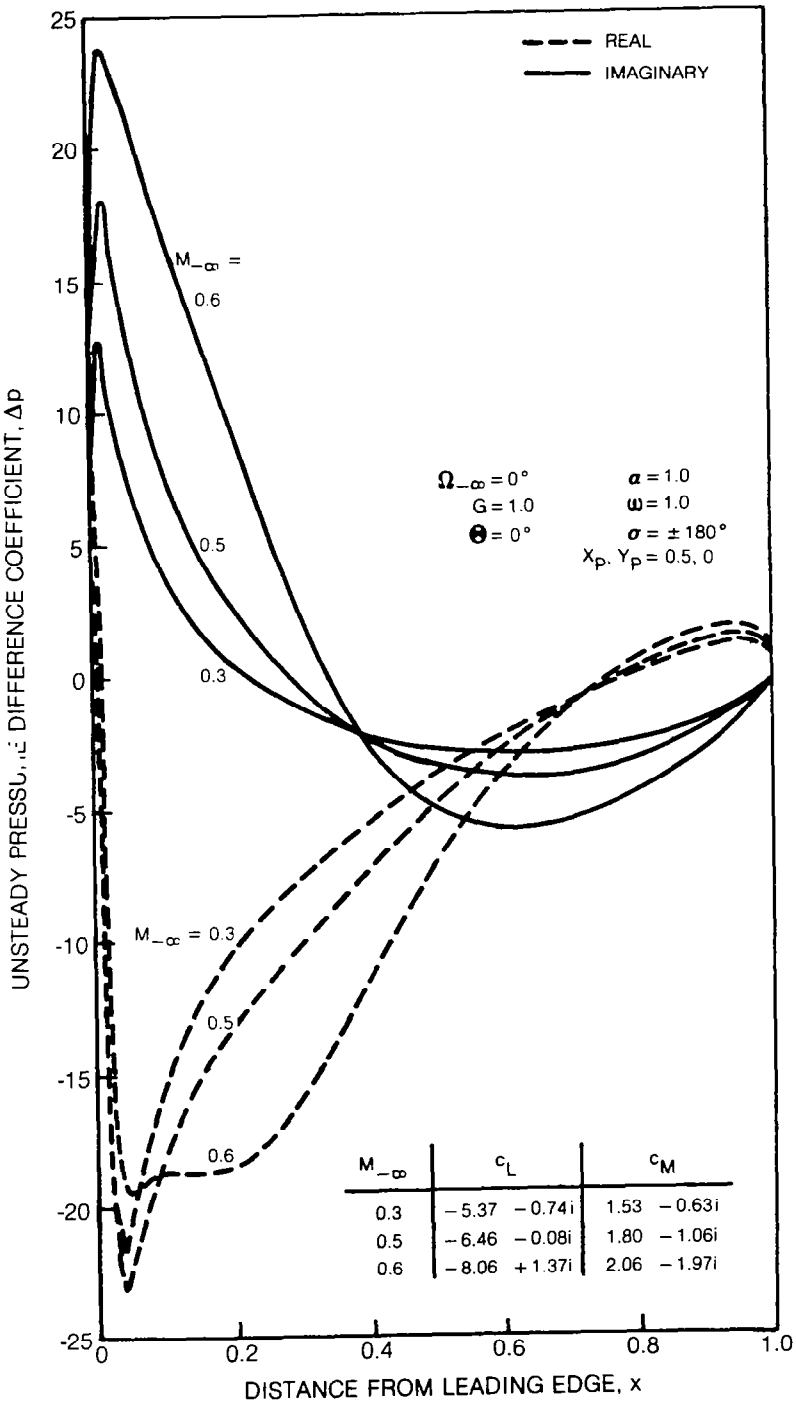

$M_{-\infty}$	c_L	c_M
0.3	−5.37 −0.74i	1.53 −0.63i
0.5	−6.46 −0.08i	1.80 −1.06i
0.6	−8.06 +1.37i	2.06 −1.97i

Fig. 9 Effect of Inlet Mach Number on Unsteady Response Due to Torsion for an Unstaggered Cascade of NACA 0012 Airfoils

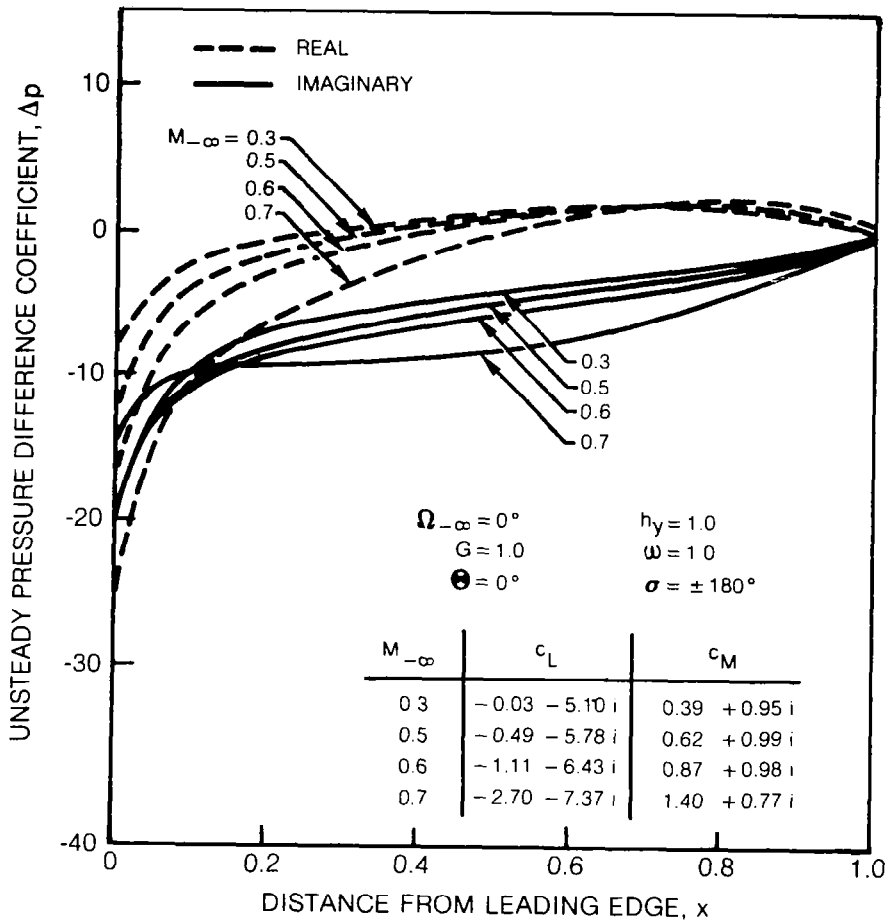

$M_{-\infty}$	c_L	c_M
0.3	−0.03 − 5.10 i	0.39 + 0.95 i
0.5	−0.49 − 5.78 i	0.62 + 0.99 i
0.6	−1.11 − 6.43 i	0.87 + 0.98 i
0.7	−2.70 − 7.37 i	1.40 + 0.77 i

Fig. 10 Effect of Mach Number on Unsteady Reponse Due to Bending for an Unstaggered Flat Plate Cascade

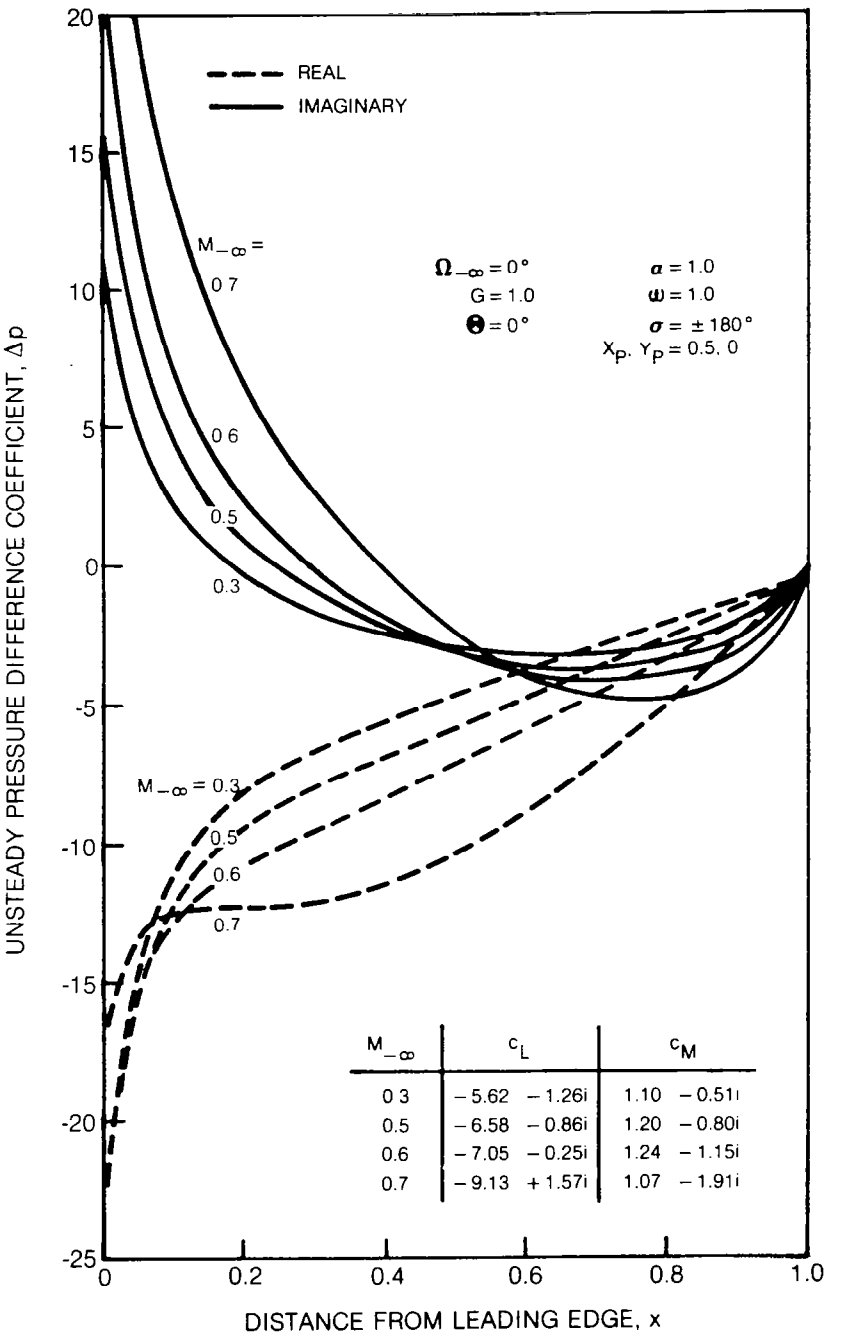

$M_{-\infty}$	C_L	C_M
0 3	− 5.62 − 1.26i	1.10 − 0.51i
0.5	− 6.58 − 0.86i	1.20 − 0.80i
0.6	− 7.05 − 0.25i	1.24 − 1.15i
0.7	− 9.13 + 1.57i	1.07 − 1.91i

Fig. 11 Effect of Inlet Mach Number on Unsteady Response Due to Torsion for an Unstaggered Flat Plate Cascade

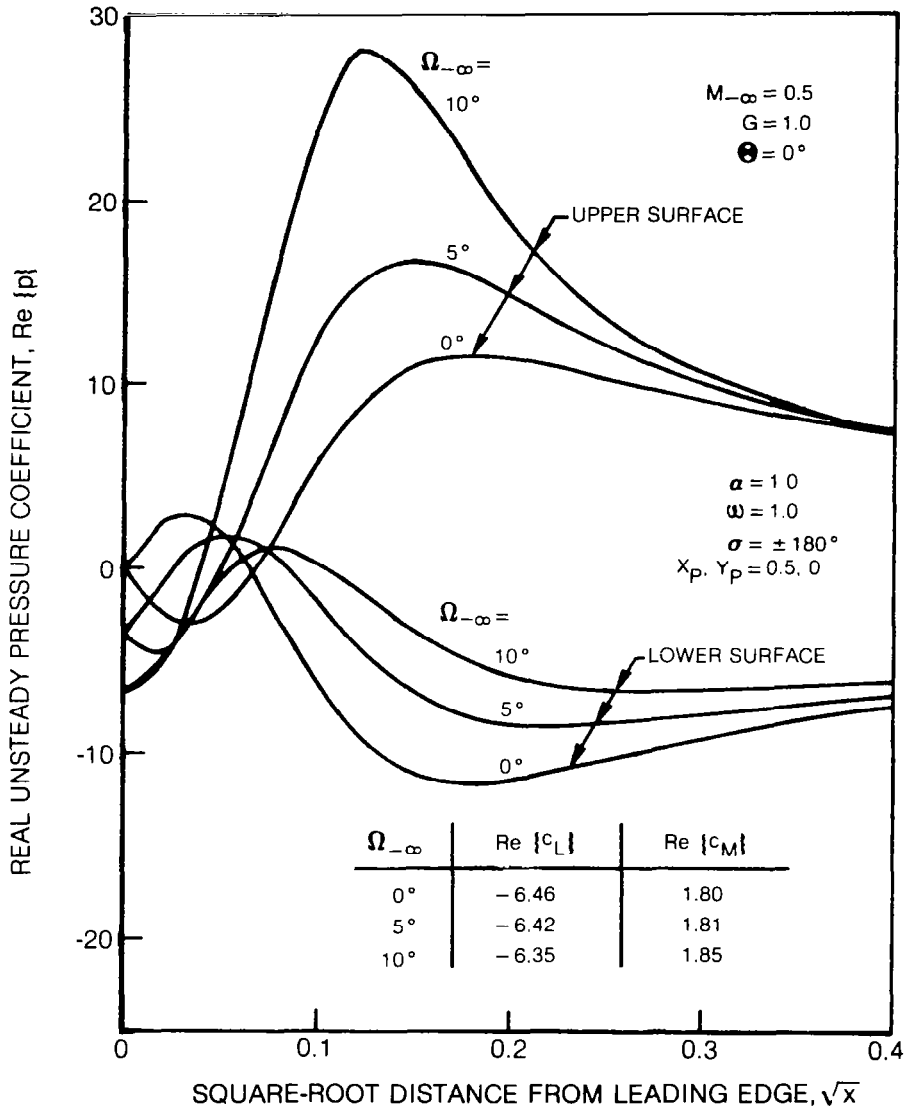

Fig. 12 Effect of Incidence on Real Pressure Distribution near the Leading Edge of a NACA 0012 Blade Due to Torsion

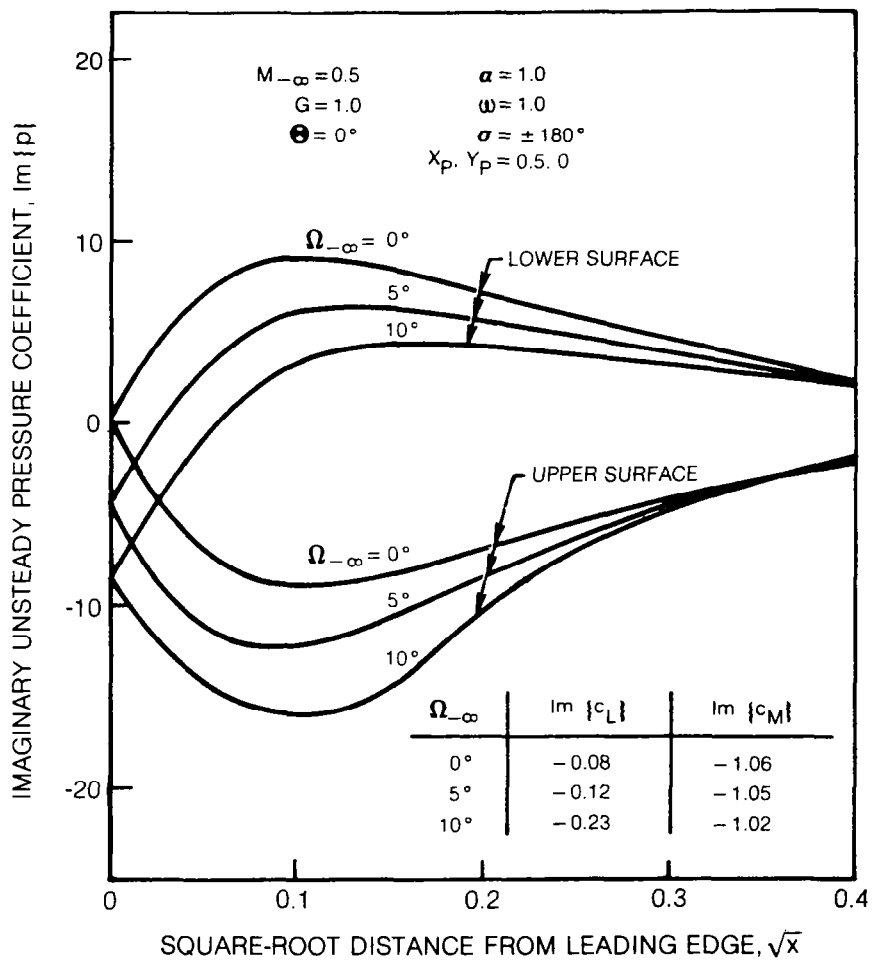

Fig. 13 Effect of Incidence on Imaginary Pressure Distribution near the Leading Edge of NACA 0012 Blade Due to Torsion

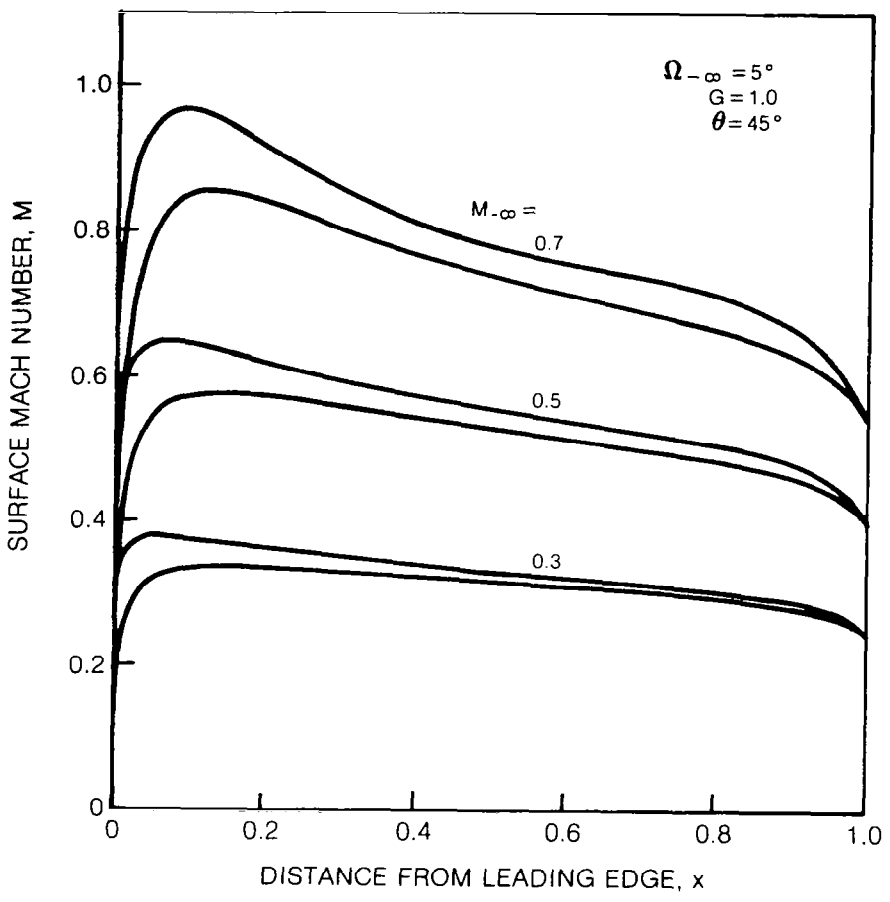

Fig. 14 Surface Mach Number Distribution for a Staggered Cascade of NACA 0012 Airfoils at Incidence

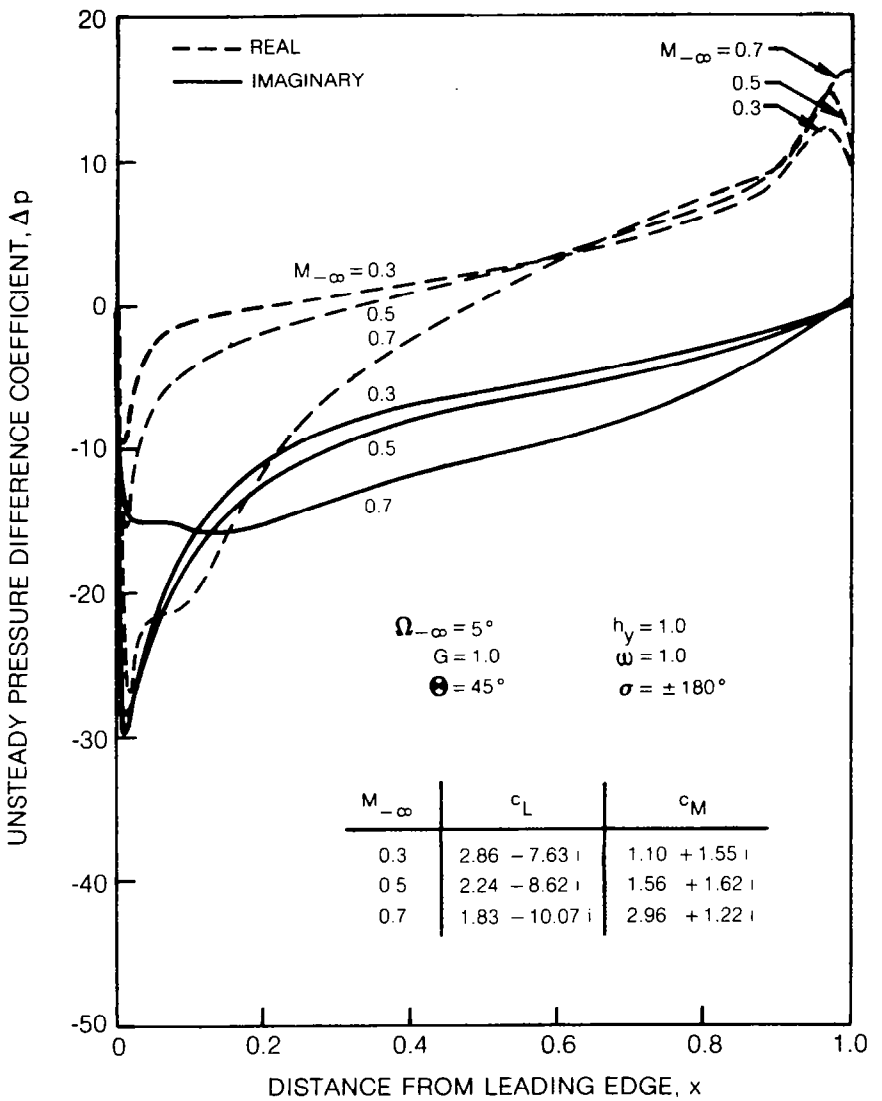

$M_{-\infty}$	c_L	c_M
0.3	2.86 − 7.63 i	1.10 + 1.55 i
0 5	2.24 − 8.62 i	1.56 + 1.62 i
0.7	1.83 − 10.07 i	2.96 + 1.22 i

Fig. 15 Unsteady Response Due to Bending for a Staggered Cascade of NACA 0012 Airfoils

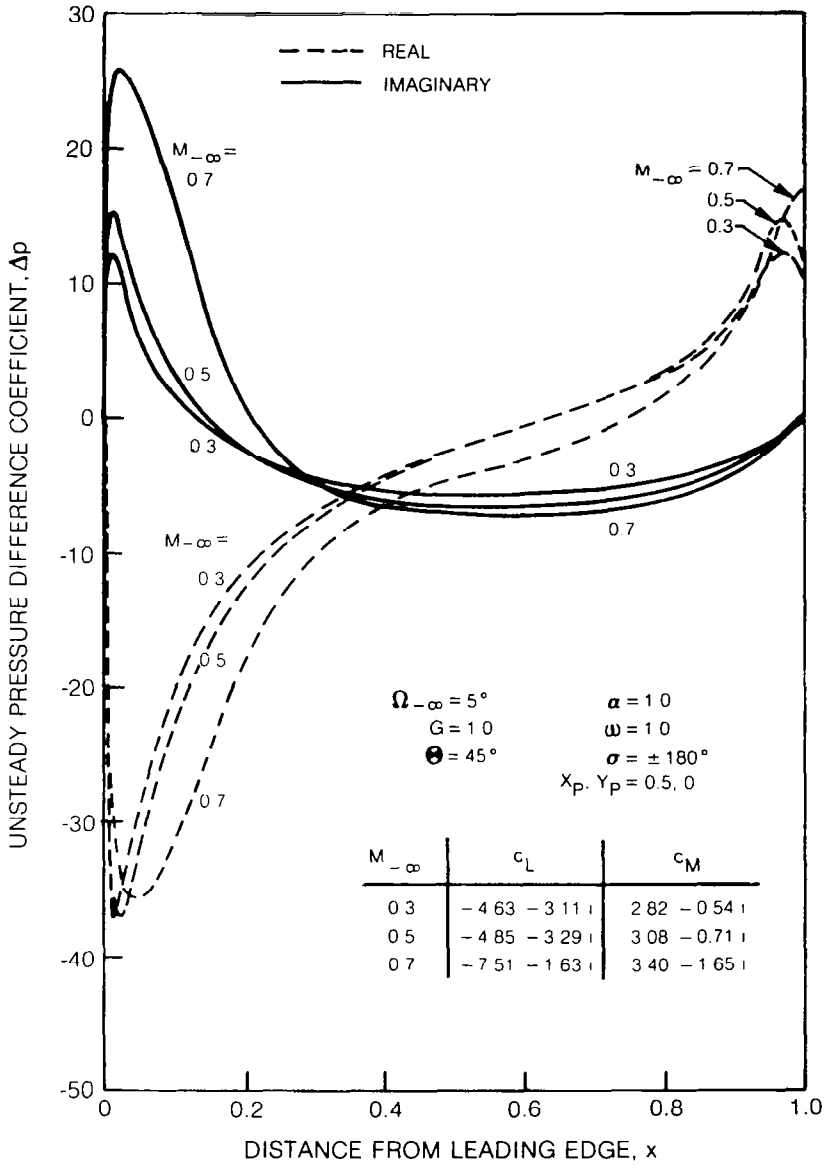

Fig. 16 Unsteady Response Due to Torsion for a Staggered Cascade of NACA 0012 Airfoils

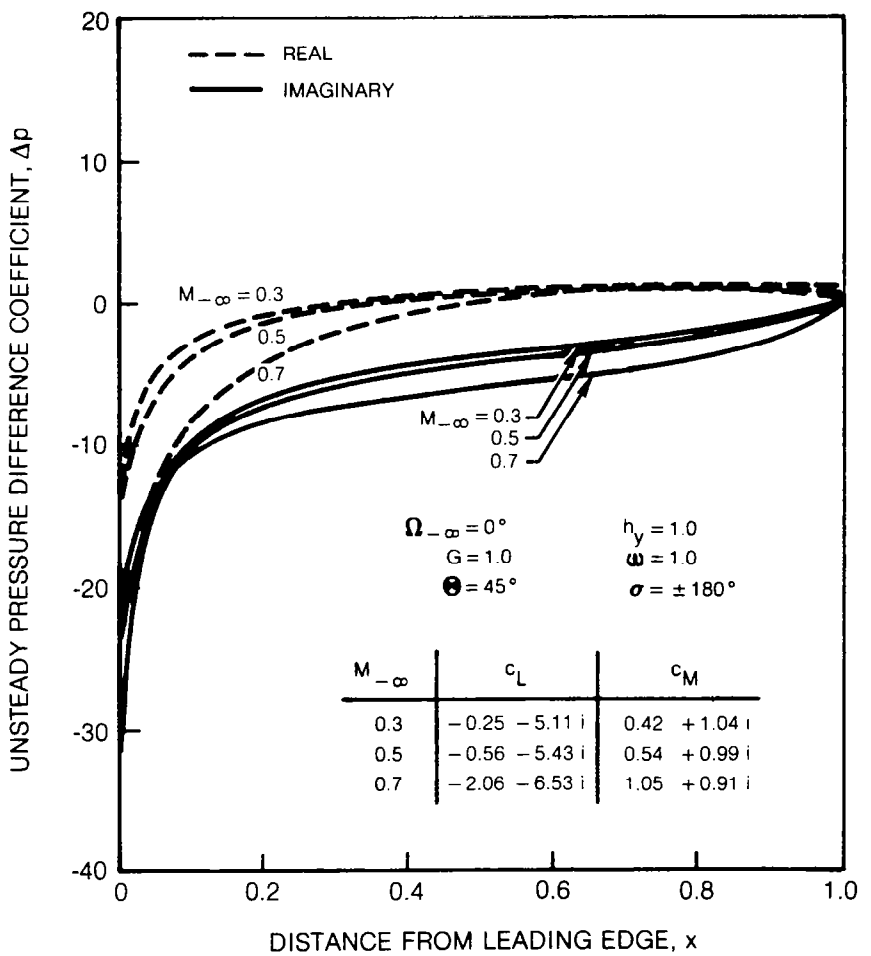

Fig. 17 Unsteady Response Due to Bending for a Staggered Flat Plate Cascade

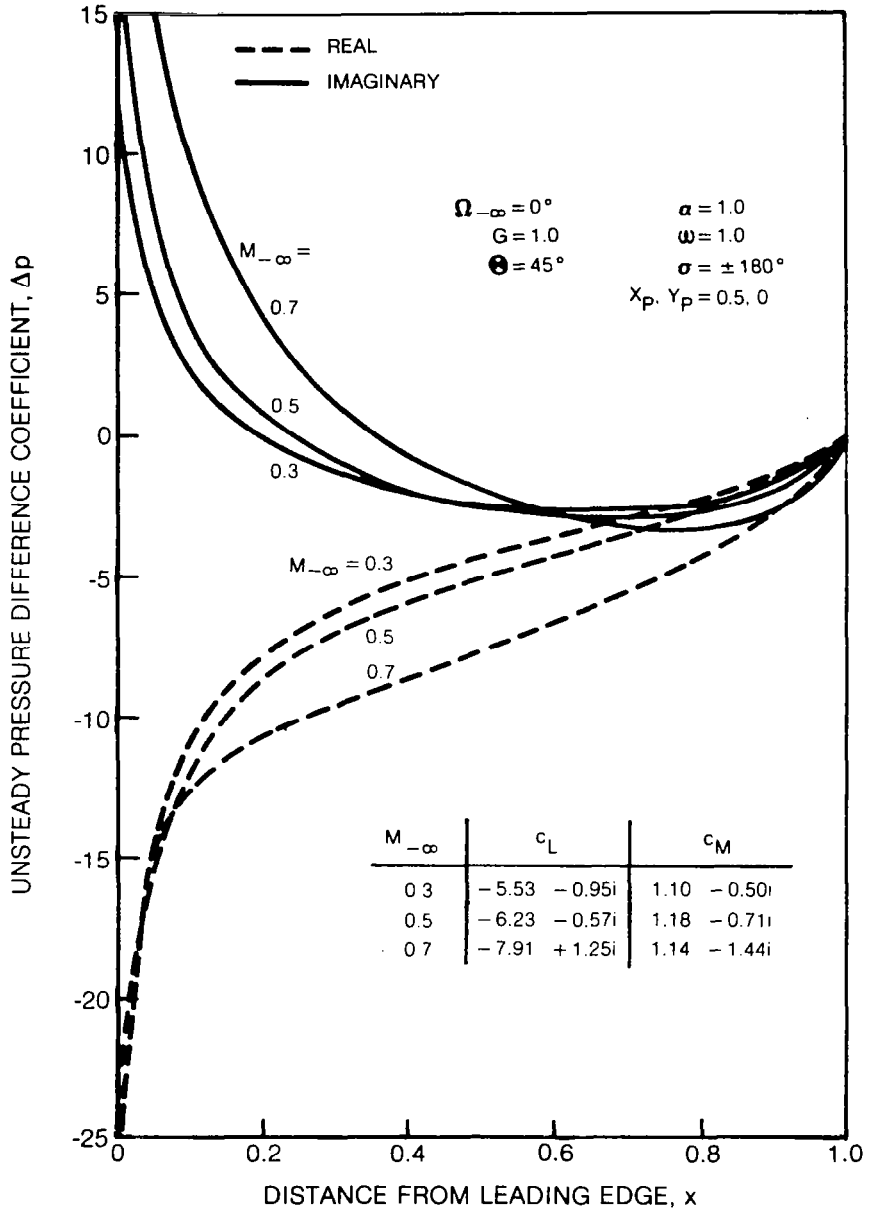

$M_{-\infty}$	c_L	c_M
0.3	−5.53 − 0.95i	1.10 − 0.50i
0.5	−6.23 − 0.57i	1.18 − 0.71i
0.7	−7.91 + 1.25i	1.14 − 1.44i

Fig. 18 Unsteady Response Due to Torsion for a Staggered Flat Plate Cascade

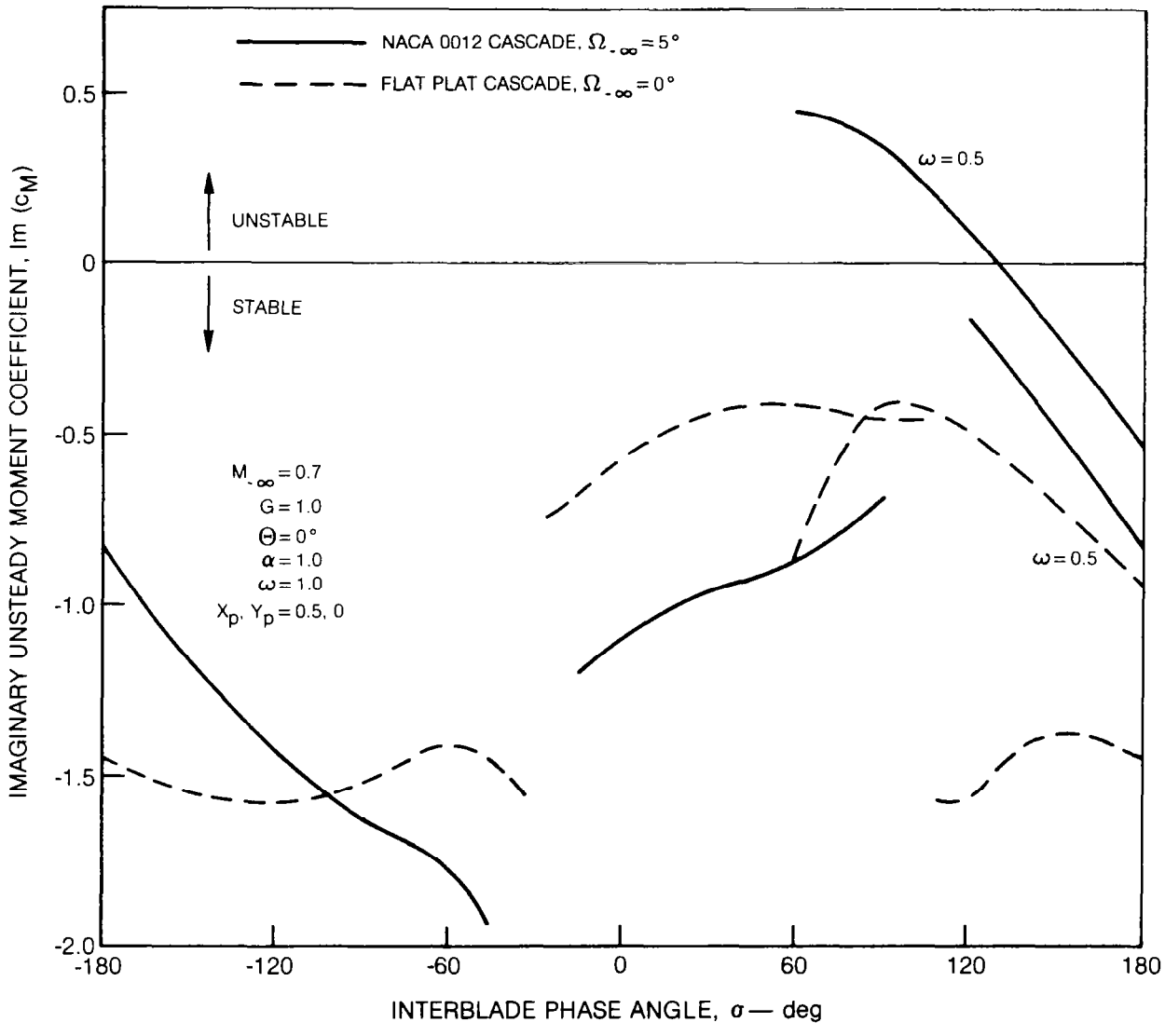

Fig. 19 Imaginary Component of Unsteady Moment Due to Torsion for Staggered Cascades

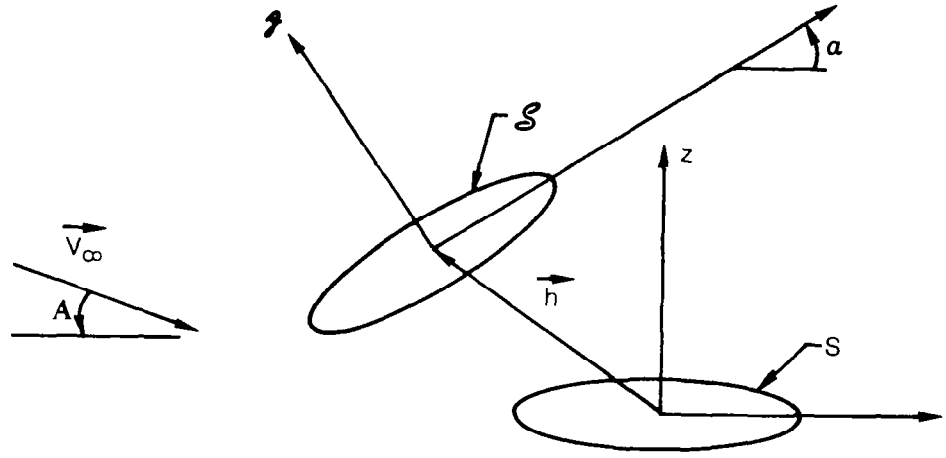

Fig. 20 Incompressible Flow Past a Displaced Elliptic Airfoil

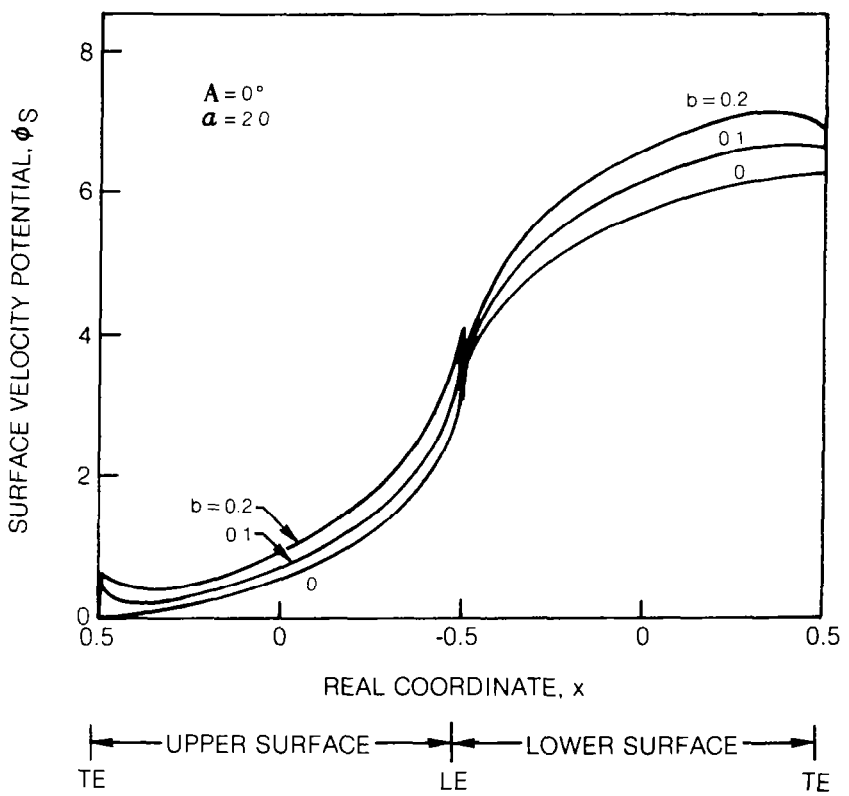

Fig. 21 First-Order Potential on Airfoil Surface for Incompressible Flow Past Flat Plate and Elliptic Airfoils

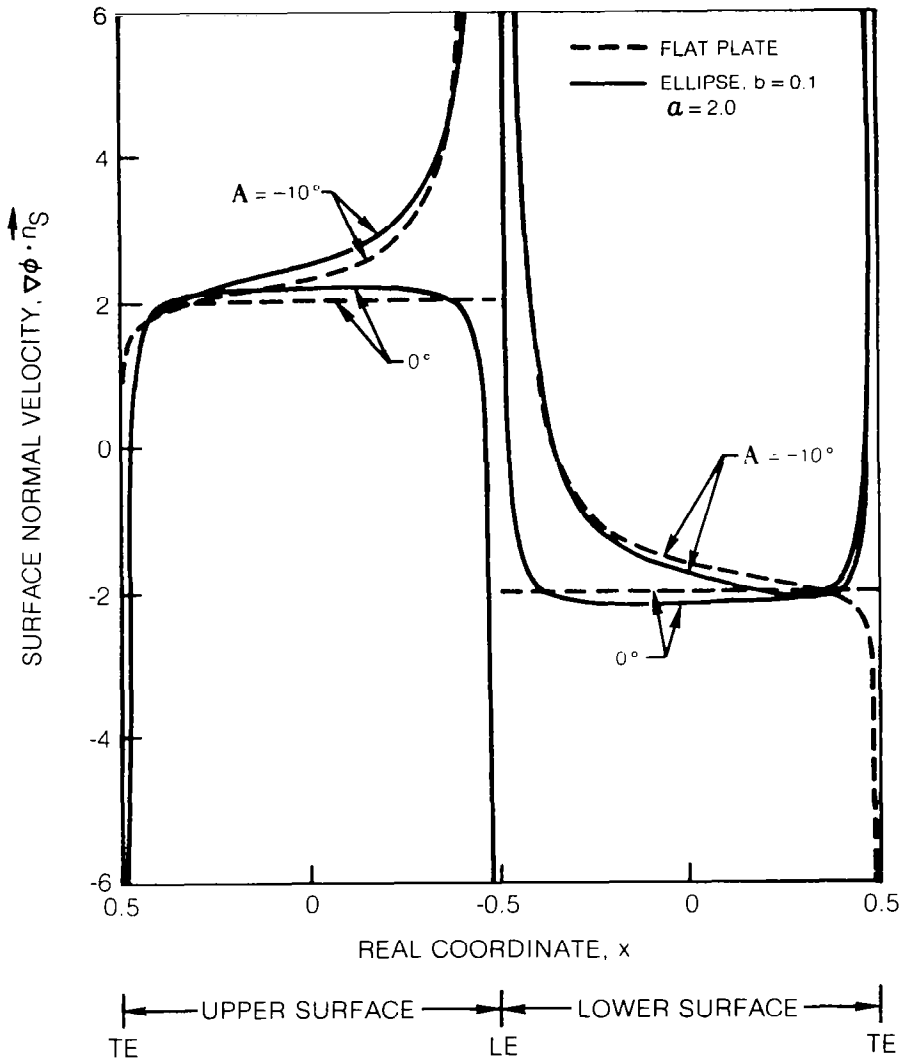

Fig. 22 First-Order Normal-Velocity on Airfoil Surface for Incompressible Flow Past Flat Plate and Elliptic Airfoils

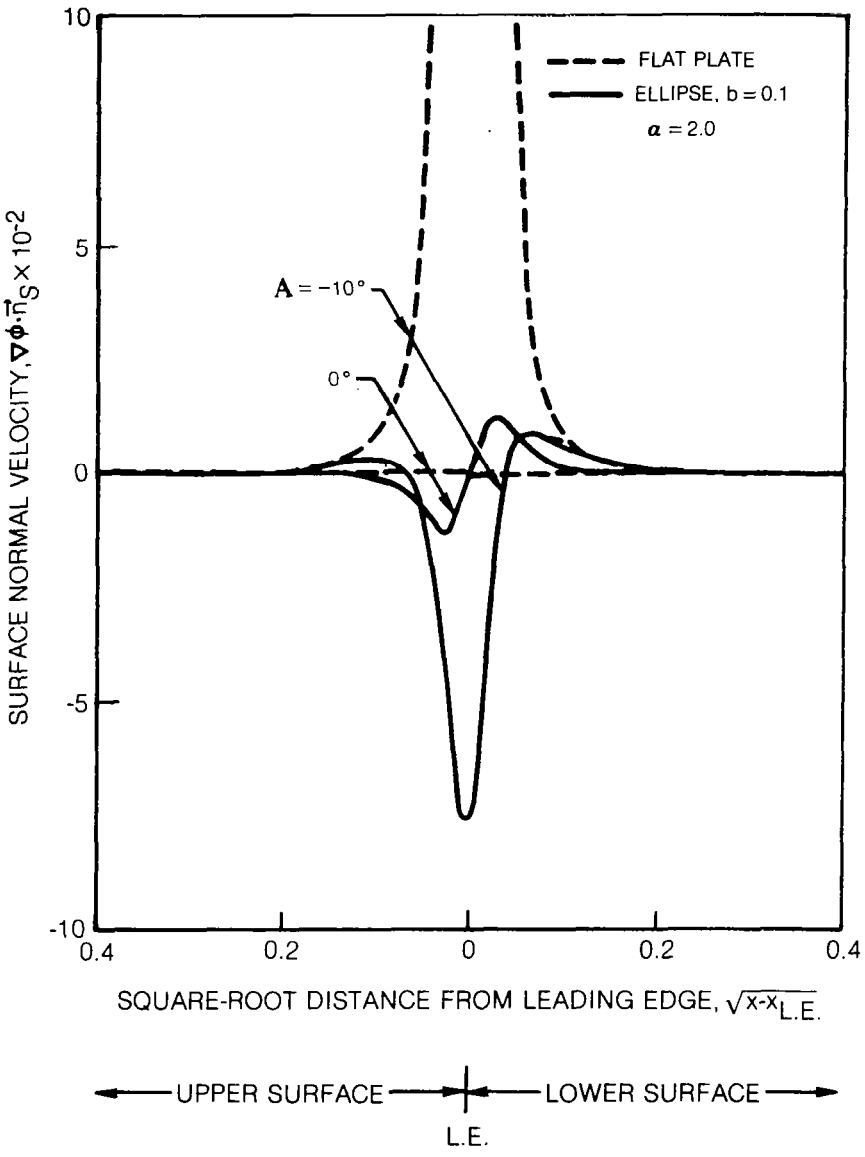

Fig. 23 First-Order Normal-Velocity on Airfoil Surface near Leading Edge for Incompressible Flow Past Flat Plate and Elliptic Airfoils

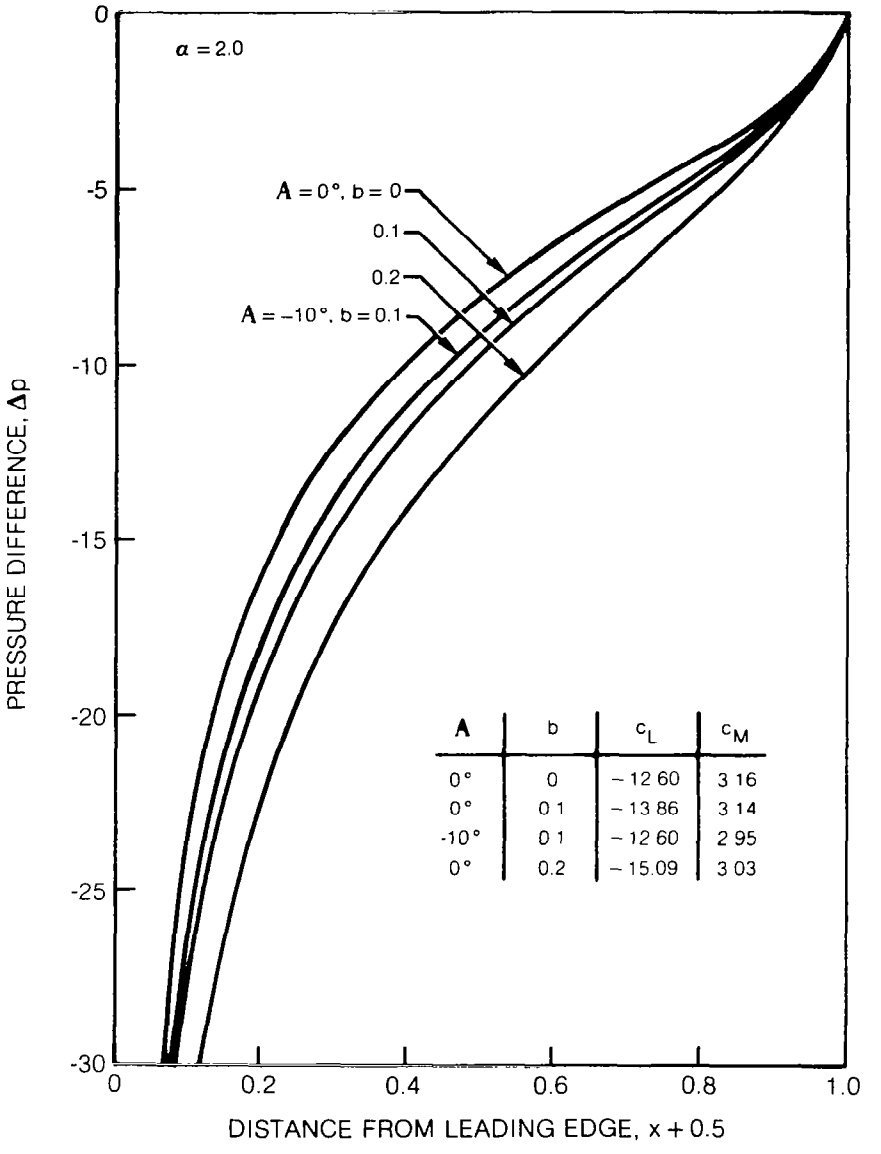

Fig. 24 First-Order Pressure Difference for Incompressible Flow Past Flat Plate and Elliptic Airfoils

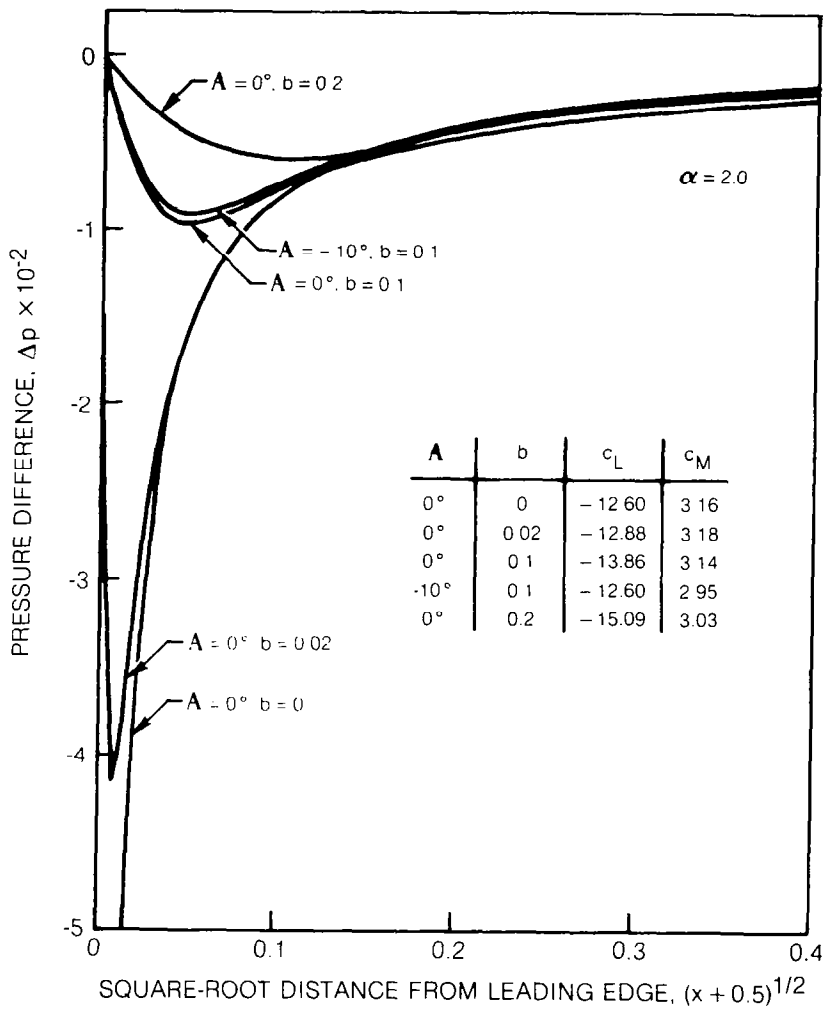

A	b	c_L	c_M
0°	0	−12.60	3.16
0°	0.02	−12.88	3.18
0°	0.1	−13.86	3.14
-10°	0.1	−12.60	2.95
0°	0.2	−15.09	3.03

Fig. 25 First-Order Pressure Difference near the Leading Edge for Incompressible Flow Past Flat Plate and Elliptic Airfoils

1. Report No.	2. Government Accession No.	3. Recipient's Catalog No.
NASA CR-3455		

4. Title and Subtitle	5. Report Date
DEVELOPMENT OF AN UNSTEADY AERODYNAMIC ANALYSIS FOR FINITE-DEFLECTION SUBSONIC CASCADES	September 1981
	6. Performing Organization Code
7. Author(s)	8. Performing Organization Report No.
Joseph M. Verdon and Joseph R. Caspar	R81-914777-7
	10. Work Unit No.
9. Performing Organization Name and Address	
United Technologies Research Center Silver Lane East Hartford, Connecticut 06108	11. Contract or Grant No. NAS3-21981
	13. Type of Report and Period Covered
12. Sponsoring Agency Name and Address	Contractor Report
National Aeronautics and Space Administration Washington, D.C. 20546	14. Sponsoring Agency Code 510-55-12

15. Supplementary Notes

Final report. Project Manager, John J. Adamczyk, Fluid Mechanics and Acoustics Division, NASA Lewis Research Center, Cleveland, Ohio 44135.

16. Abstract

An unsteady potential flow analysis, which accounts for the effects of blade geometry and steady turning, is being developed to predict aerodynamic forces and moments associated with free-vibration or flutter phenomena in the fan, compressor, or turbine stages of modern jet engines. Based on the assumption of small-amplitude blade motions, the unsteady flow is governed by linear equations with variable coefficients which depend on the underlying steady flow. These equations are approximated using difference expressions determined from an implicit least-squares development and applicable on arbitrary grids. The resulting linear system of algebraic equations is block tridiagonal, which permits an efficient, direct (i.e., noniterative) solution. In previous work unsteady solutions were obtained on a rectilinear-type, nonorthogonal, body-fitted, and periodic grid (termed "the cascade mesh") for cascades of sharp-edged airfoils aligned with the steady flow. Under the present effort the solution procedure has been extended to treat blades with rounded or blunt edges at incidence relative to the inlet flow. As part of this effort analytical studies in the vicinity of blade edges. Further, the numerical approximation has been applied to determine unsteady solutions for blunt leading-edged blades on the cascade mesh and on a dense "local" mesh surrounding the leading edge. Sample results are presented for NACA 0012 and flat plate cascades to illustrate the effects of blade geometry, inlet Mach number, and inlet flow angle on unsteady response.

17. Key Words (Suggested by Author(s))	18. Distribution Statement
Unsteady aerodynamics; Small-amplitude potential; Subsonic; Implicit least squares; Finite-deflection; Cascade mesh; Blunt leading edge; Local mesh; Nonuniform mean flow; Block tridiagonal	Unclassified - unlimited STAR Category 02

19. Security Classif. (of this report)	20. Security Classif. (of this page)	21. No. of Pages	22. Price*
Unclassified	Unclassified	76	A05

* For sale by the National Technical Information Service, Springfield, Virginia 22161

NASA-Langley, 1981